INSTITUTE OF NATURAL AND APPLIED SCIENCES
UNIVERSITY OF CUKUROVA

PhD THESIS

Banu ÖZEL

STUDY OF THE 112,120Sn (g,g) REACTION AND SYSTEMATICS OF THE PYGMY DIPOLE RESONANCE AT THE Z=50 SHELL CLOSURE

DEPARTMENT OF PHYSICS

ADANA, 2008

ÇUKUROVA ÜNİVERSİTESİ

FEN BİLİMLERİ ENSTİTÜSÜ

112,120Sn(g,g) REAKSİYONU VE Z=50 KAPALI KABUKLARINDA PYGMY DİPOL REZONANSI SİSTEMATİĞİNİN İNCELENMESİ

Banu ÖZEL

DOKTORA TEZİ
FİZİK ANABİLİM DALI

Bu tez 28.01.2008 tarihinde aşağıdaki jüri üyeleri tarafından oybirliği ile kabul edilmiştir.

İmza...........................
Prof.Dr. Süleyman GÜNGÖR
1. DANIŞ MAN

İmza............................
Prof.Dr. Peter von NEUMANN-COSEL
2. DANIŞ MAN

İmza...........................
Prof.Dr. Metin ÖZDEMİR
ÜYE

İmza............................
Prof.Dr. Sefa ERTÜRK
ÜYE

İmza............................
Prof.Dr. Gülsen ÖNENGÜT
ÜYE

Bu tez Enstitümüz Fizik Anabilim Dalında hazırlanmıştır.
Kod No:

Prof.Dr. Aziz ERTUNÇ
Enstitü Müdürü
İmza ve Mühür

ÖZ

DOKTORA TEZİ

112,120Sn(g,g) REAKSİYONU VE Z=50 KAPALI KABUKLARINDA PYGMY DİPOL REZONANSI SİSTEMATİĞİNİN İNCELENMESİ

Banu ÖZEL

ÇUKUROVA ÜNİVERSİTESİ
FEN BİLİMLERİ ENSTİTÜSÜ
FİZİK ANABİLİM DALI

Bu tezde S DALINAC süper iletken elektron lineer hızlandırıcısında gerçekleştirilen 112,120Sn(g,g) reaksiyonları Bremsstrahlung spektrumunun farklı son nokta enerjileri için nötron ayrışma enerjisinin altındaki bölgelerde çalışılmıştır. 112Sn çekirdeği için 9.5 MeV ye, 120Sn çekirdeği için 7.5 ve 9.1 MeV ye kadar dipol geçiş şiddetleri dağılımı oluşturulmuştur. Elde edilen sonuçlar hali hazırda varolan 116,124Sn (Govaert, ve ark., 1998) verileri ile birlikte nötron fazlalığı olan çekirdeklerde bulunan pygmy dipol rezonansı olarak adlandırılan yapı hakkında bilgi edinmemizi sağlamıştır. Buna ek olarak parçalanma analizi denilen bir analiz metodu foton saçılması ile elde edilmiş olan spektrumlara, parçalanmadan kaynaklanan ve fonda bulunan çözülmemiş geçiş şiddetlerinin miktarlarını tahmin edebilmek amacıyla uygulanmıştır.

Sonuçlar quasiparticle phonon modeli ve relativistik quasiparticle RPA ile karşılaştırılmıştır.

ABSTRACT

PhD THESIS

STUDY OF THE 112,120Sn (g,g) REACTION AND SYSTEMATICS OF THE

PYGMY DIPOLE RESONANCE AT THE Z=50 SHELL CLOSURE

Banu ÖZEL

DEPARTMENT OF PHYSICS
INSTITUTE OF NATURAL AND APPLIED SCIENCES
UNIVERSITY OF ÇUKUROVA

Supervisor: Prof.Dr. Süleyman GÜNGÖR
2. Supervisor: Prof.Dr. Peter von NEUMANN-COSEL
Year: 2008, Pages: 75
Jury: Prof.Dr. Süleyman GÜNGÖR

Prof.Dr. Peter von NEUMANN-COSEL
Prof.Dr. Metin ÖZDEMİR
Prof.Dr. Sefa ERTÜRK
Prof.Dr. Gülsen ÖNENGÜT

In this thesis the 112,120Sn(g,g) reactions are studied at different endpoint energies of the incident bremsstrahlung spectrum below the neutron separation energies at the superconducting Darmstadt electron linear accelerator S DALINAC. Dipole transition strength distributions are extracted for 112Sn up to 9.5 MeV and for 120Sn up to 9.1 MeV. A concentration of dipole excitations is observed between 5 and 8 MeV. Furthermore a fluctuation analysis is applied to the photon scattering spectra to estimate the amount of the unresolved strength hidden in background due to fragmentation of the strength. Together with existing data for 116,124Sn (Govaert, et al., 1998) this provides a set of information on the structure of the so-called pygmy dipole resonance (PDR) in the stable neutron-rich tin nuclei.

The results are compared to microscopic quasiparticle-phonon model and relativistic quasiparticle RPA calculations.

Key Words: Pygmy Dipole Resonance, E1 transition strength, Nuclear Resonance Fluorescence, fluctuation analysis

ACKNOLEDGEMENTS

TABLE OF CONTENTS **PAGE**

LIST OF TABLES PAGE

LIST OF FIGURES   **PAGE**

LIST OF SYMBOLS AND ABBREVIATIONS

A	Mass number
Z	Proton number
N	Neutron number
J	Spin
γ	Gamma radiation
β	Beta radiation
GDR	Giant Dipole Resonance
PDR	Pygmy Dipole Resonance
GMR	Giant Monopole Resonance
GQR	Giant Quadrupole Resonance
$S-DALINAC$	Superconducting Darmstadt electron linear accelerator
$QCLAM$	Quadrupole-clamshell magnetic spectrometer
GSI	Geselschaft für Schwerionenforschung mbH
NRF	Nuclear Resonance Fluorescence
$GEANT4$	Simulation program
$E1$	Electric dipole transition
$EWSR$	Energy-weighted sum rule
TRK	Thomas-Reiche-Kuhn
RPA	Random phase approximation
$QRPA$	Quasiparticle random phase approximation
QPM	Quasiparticle phonon model
DFT	Density fluctuation theory
$DD-ME$	Density dependent meson exchange
$ETFFS$	Extended theory of finite fermion systems
$HPGe$	High purity germanium detector
BGO	$Bi_4Ge_3O_2$
ESS	Escape suppresed spectrometer
SE	Single escape
DE	Double escape
λ	multipolarity

$B(E1)$	Reduced transition probability of an electric dipole transition
$B(M1)$	Reduced transition probability of a magnetic dipole transition
$B(E2)$	Reduced transition probability of an electric quadrupole transition
Γ	Width
E_x	Excitation energy
E_γ	Photon energy
σ	Cross section
I	Integrated cross section
g	statistical g factor
N_γ	Photon flux
ε_{abs}	Absolute efficiency
M	Mass of nucleus
ν	Velocity of nuclei
θ	Theta, angle
Δ	Doppler width
e	Electron charge
$\hbar$	Planck constant/2π
π	Pi number
μA	Microampere
c	Speed of light
k	Boltzmann constant
fm	Femtometer
meV	Millielectronvolt
keV	Kiloelectronvolt
MeV	Megaelectronvolt
K	Kelvin
T	Temperature
$P_\lambda(\Theta)$	Legendre polynomial function
$W(\theta)$	Angular correlation function

NLD	Nuclear level density
σ	Spin cut-off parameter
a	Level density parameter
M_{LD}	Microscopic liquid-drop mass
$BSFG$	Back shifted fermi gas model
$HF-BCS$	Hartree Fock BCS model
$<D>$	Mean level spacing
$<\Gamma>$	Mean level width
β	One of BSFG free parameters
γ	One of BSFG free parameters
α	One of BSFG free parameters
ΔE	Energy resolution
$C(\varepsilon)$	Autocorrelation function
ε	shift parameter

1. INTRODUCTION

Many experimental and theoretical studies have been performed to get detailed information about electric dipole excitations in nuclei. In heavy nuclei we can divide this type of excitations into three groups. A typical example of collective excitation is the isovector Giant Dipole Resonance (GDR), a mode interpreted as oscillation of neutrons and protons against to each other, which has been extensively studied (Berman et al.,1975). The GDR is located at energies between 14 MeV (Uranium) and 26 MeV (Lithium) (Dietrich et al., 1988) and it exhausts nearly 100% of the E1 isovector energy weighted sum rule (EWSR). In neutron rich nuclei it was suggested within the hydrodynamical model that another type of dipole resonance might exist in the energy region below the GDR. This mode, known as the Pygmy Dipole Resonance (PDR) corresponds to the vibration of the neutron skin against the proton-neutron core with $N \approx Z$ (Mohan et al., 1971). In stable nuclei, low-lying E1 excitations have been known for a long time (Bartholomev et al., 1972) but their nature and systematic features were poorly understood. In particular, the results were not compatible with the predictions of (Mohan et al., 1971). Thus, the possible existence of a PDR remained a subject of debate. Low energy electric dipole transitions are currently a topic of high interest, caused by recent significant experimental progress in studies of their properties in stable as well as in exotic neutron rich nuclei. The low-energy E1 strength in stable targets has been extensively studied in (γ, γ') scattering below the neutron separation energies over the last decades (Hartmann et al., 2004; Hartmann et al., 2000; Enders et al., 1998, 2000, 2003; Zilges et al., 2002; Volz et al. 2006; Ryezayeva et al., 2002, Govaert et al., 1998; Schwengner et al., 2007).

The aim of the present study is to establish systematics of PDR at Z=50 shell closure in stable tin isotopes. This work establishes the existence of a cumulation of E1 strength, typically close to the particle threshold. The tin isotopic chain is a very interesting case to study because it allows a large variation of the neutron number. It has also been studied in great detail by theory (Tsoneva et al., 2004; 2007; Paar et al., 2003; 2005; Piekarewicz, 2006; Terasaki et al., 2005) and can thus serve as a benchmark test for a variety of models. We report on a high resolution nuclear resonance fluorescence (NRF) study of electric dipole strength in ^{112}Sn and ^{120}Sn. The experiments have been performed at Darmstadt electron linear accelerator, S-DALINAC. For the understanding of the systematics fea-

tures, the data on ^{116,124}Sn are adopted from a previous work (Govaert et al., 1998). Figure 1.1 shows the measured even tin isotopes from mass 112 to 132 and indicates the

Gent

112Sn	116Sn	120Sn	124Sn		130Sn	132Sn
STABLE	STABLE	STABLE	STABLE	...	3.72 M	39.7 S
0.97%	14.54%	32.58%	5.79%		β⁻	β⁻

Darmstadt   GSI
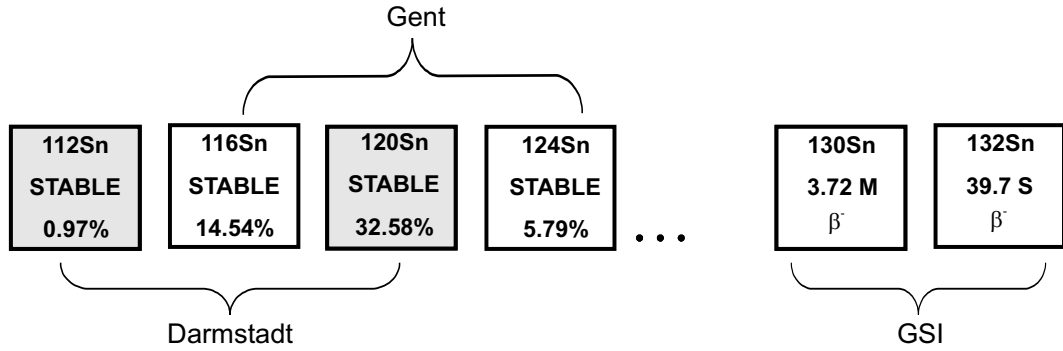
Figure 1.1   Measured even-even isotopes in the tin isotopic chain

available measured data. Coulomb dissociation experiments have been performed at GSI (Gesellschaft für Schwerionenforschung) to provide data on the E1 strength in unstable ^{130,132}Sn (Adrich et al., 2005) and neighboring odd nuclei (Klimkiewicz et al., 2007) above neutron threshold.

Beyond the analysis of resolved transitions, in the present work a fluctuation analysis is applied to (γ, γ') spectra of ^{112}Sn and ^{120}Sn to investigate the amount of unresolved E1 strength which might be hidden in the background because of the fragmentation of the strengths due to the high level density. The main idea of this method is to determine the experimental background of spectra with the help of the autocorrelation function.

The results of low-lying E1 states in stable tin isotopes is compared to microscopic calculations such as quasiparticle phonon model (QPM), quasiparticle random phase approximation (QRPA) and relativistic quasiparticle random phase approximation (R QRPA) which allow to draw some conclusion on the predictive power of different models as well as the nature of the PDR mode in tin isotopes.

2. PREVIOUS WORKS

The study of the photoresponse with (γ, γ') experiments has been extended in recent years to many other nuclei beyond the $Z=50$ region. In particular, the PDR has been observed in ^{44,48}Ca (Hartmann et al., 2004; Hartmann et al., 2000), ^{52}Cr (Enders et al., 1998), ^{56}Fe and ^{58}Ni (Bauwens et al., 2000), ^{88}Sr (Schwengner et al., 2007; Kübler et al.,

Table 2.1   Results of ^{112}Sn with 9.5 MeV End-point energy

Isotope	$\sum$B(E1)(10^{-3} e^2fm^2)	% IVEWSR	E_C (MeV)
^{40}Ca	5.1(8)	0.02	6.8
^{44}Ca	92.2(156)	0.39	7.1
^{48}Ca	68.7(75)	0.33	8.4
^{48}Ti	46(19)	0.19	7.4
^{52}Cr	22.8(38)	0.09	7.8
^{56}Fe	60.2(31)	0.29	7.2
^{58}Ni	60.7(34)	0.24	5.8
^{70}Ge	34.5(75)	0.08	5.9
^{72}Ge	67.7(71)	0.16	6.4
^{74}Ge	92.7(125)	0.21	6.5
^{76}Ge	75.8(128)	0.19	6.8
^{88}Sr	122.5	0.27	7.0
^{116}Sn	233(28)	0.16	6.7
^{124}Sn	379(45)	0.27	7.0
^{138}Ba	676(118)	0.89	6.5
^{140}Ce	307(59)	0.38	6.3
^{142}Nd	184(35)	0.22	6.1
^{144}Sa	207(37)	0.23	5.7
^{208}Pb	1095(60)	0.92	6.2
^{130}Sn	3200(1370)	10.1	6.8
^{132}Sn	1900(1425)	9.8	6.8

2004; Wienhard et al., 1981; Isoyama et al., 1980), ^{92,98,100}Mo (Schwengner et al., 2007), ^{116,124}Sn (Govaert et al., 1998), N=82 isotones (Herzberg et al., 1997; Herzberg et al., 1999; Zilges et al., 2002; Volz et al. 2006) and ^{204,206,207,208}Pb (Ryezayeva et al., 2002; Chapuran et al., 1980; Enders et al., 2000; Enders et al., 2003). In all cases, a concentration of electric dipole strength exhausting up to 1 % of the EWSR was observed below the neutron threshold. These results are summarized in Table 2.1. The NRF method is restricted to stable nuclei and excitation energies roughly up to neutron separation energy. In addition, the advent of beams of radioactive exotic nuclei allows the study of Coulomb dissociation of neutron-rich nuclei in inverse kinematics (Aumann, 2006) for example at the LAND setup at GSI. This method has been used already to measure dipole strength in the exotic semi-magic ^{130}Sn, the double magic ^{132}Sn (Adrich et al., 2005) and their neighboring odd-mass isotopes (Klimkiewicz et al., 2007). The extraction of E1 strength was possible only above the neutron separation energies. The results for ^{130,132}Sn, which are listed in the lower part of Table 2.1, are 5-8 times higher than the results for the most neutron-rich stable ^{124}Sn isotope.

3. MATERIAL and METHOD

3.1   Collective Excitations in Nuclei

3.1.1   Giant Resonances

Giant resonance is a term generally used to describe collective vibrations of nuclei, which shows up as broad resonances at energies tens of MeV above the ground state. The reason that these excitations are called "giant" resonances comes from the fact that both their total strength and their widths are much larger than typical resonances built on single-particle (non-collective) excitations (Wong, 1990).

3.1.1.1   Classification of Giant Resonances

Giant resonances correspond to a collective motion involving many particles in the nucleus. The occurrence of such a collective motion is a common feature of many-body quantum systems. The term "collective" here means that the majority of the nucleons participate in the excitation. In quantum mechanical terms the resonance corresponds to a transition between ground state and a collective state and the strength of the transition will depend on the basic properties of the response and the size of the system. This implies that the total transition strength should be limited by a sum rule which depends only on ground state properties (Bohr and Mottelson, 1975). If the transition strength of an observed resonance exhausts a major part, say greater than 50% of the corresponding sum rule we call it a giant resonance. Within the liquid-drop model giant resonances ban be classified according to their angular momentum, L, isospin, T, and spin, S, as illustrated in Fig. 3.1.

- The Giant Monopole Resonance (GMR), $L = 0$, the so-called breathing mode.

- The Giant Dipole Resonance (GDR), $L = 1$ is a density/shape oscillation for the isovector case

- The Giant Quadrupole Resonance (GQR) is a surface oscillation with angular momentum $L = 2$.
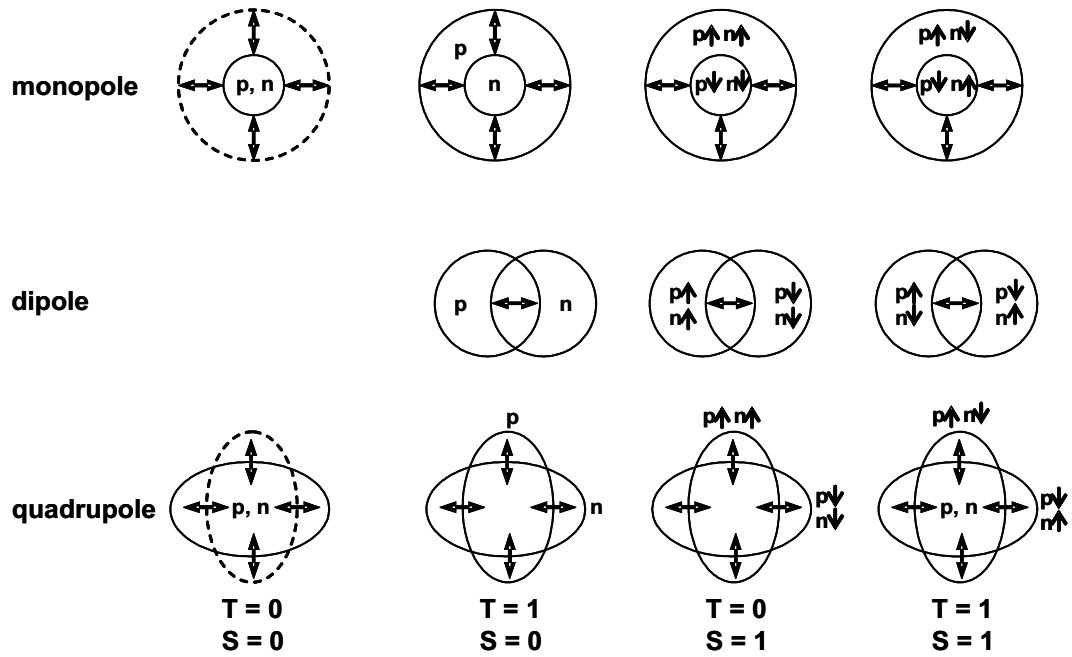
Figure 3.1   Classification of giant resonances based on a macroscopic picture (Adrich, 2005)

- According to isospin, T, the modes are classified as:

- Isoscalar ($\Delta T = 0$) - in which neutrons oscillate in phase with protons

- Isovector ($\Delta T = 1$) - in which neutrons and protons oscillate with opposite phase

  For the same multipolarity the vector modes are always higher in excitation energy than the isoscalar ones, since the separation of proton and neutron distributions requires additional energy. But the GDR is an exception and the isovector mode is lower in energy because the ISGDR is a second-order mode. The fundamental mode is spurious; it corresponds to a translative motion of the nucleus as a whole.

  The shape of ISGDR mode is not shown in Fig. 3.1 because it is a more complex compressional mode which does not have a simple macroscopic illustration.

- According to the spin S, the modes are classified as:

- Electric ($\Delta S = 0$) - in which nucleons vibrate following a multipole pattern given by L.

- Magnetic ($\Delta S = 1$) - in which nucleons with spin up vibrate against nucleons with spin down, following a multipole pattern given by L.
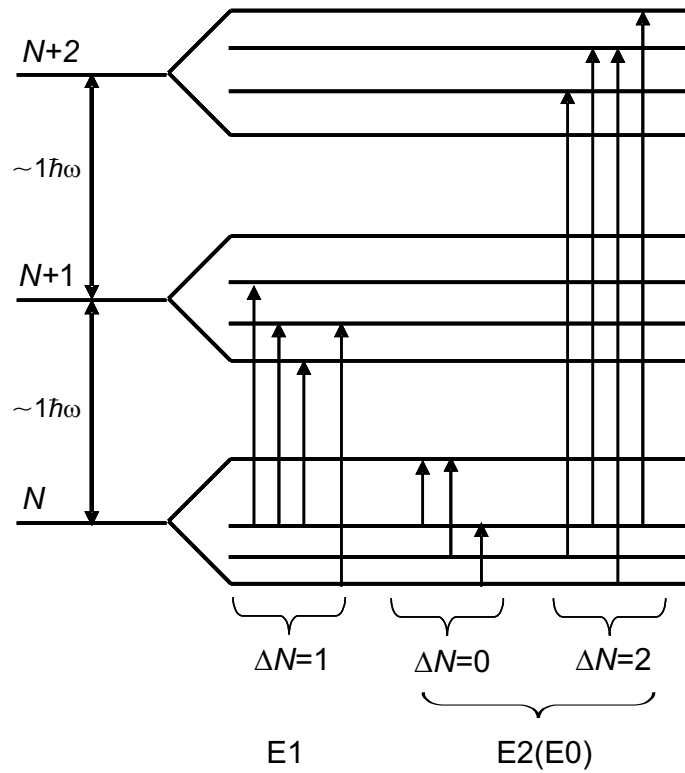
Figure 3.2   Schematic picture of E1 and E2(E0) single-particle transition between shell-model states (Harakeh, 2001).

From a microscopic point of view, giant resonances can be described as a coherent superposition of particle-hole (1p-1h) excitations resulting from the operation on the ground state. The qualitative features of giant resonances can be understood by considering a schematic shell-model picture in Fig. 3.2. Well-known features of this model are that the parity of the single-particle wave functions in subsequent oscillator shells N, $N+1$, $N+2$,... is alternating and that their energy difference $\Delta E = \Delta N \times 1\hbar\omega = \Delta N \times 41A^{-1/3}$ MeV (Harakeh, 2001). For the quadrupole case, the $\Delta N = 0$ transitions form low-energy collective phonons while $\Delta N = 2$ transitions correspond to the giant resonance.

According to the microscopic interpretation of the IVGDR the energy centroid is in fact higher than $1\hbar\omega$. This is a feature of the repulsive isovector residual interaction which pushes all the E1 strength to higher energies (and very little is found at low energies (Brown, et al.,1959).

3.1.2 Electric Dipole Excitations in Nuclei

Throughout the last decade numerous experiments using electromagnetic probes have provided a vast amount of data on low-lying electric dipole excitations in heavy nuclei. Generally electric dipole excitations in these nuclei can be divided into three structurally different groups which are shown schematically in Fig 3.3.
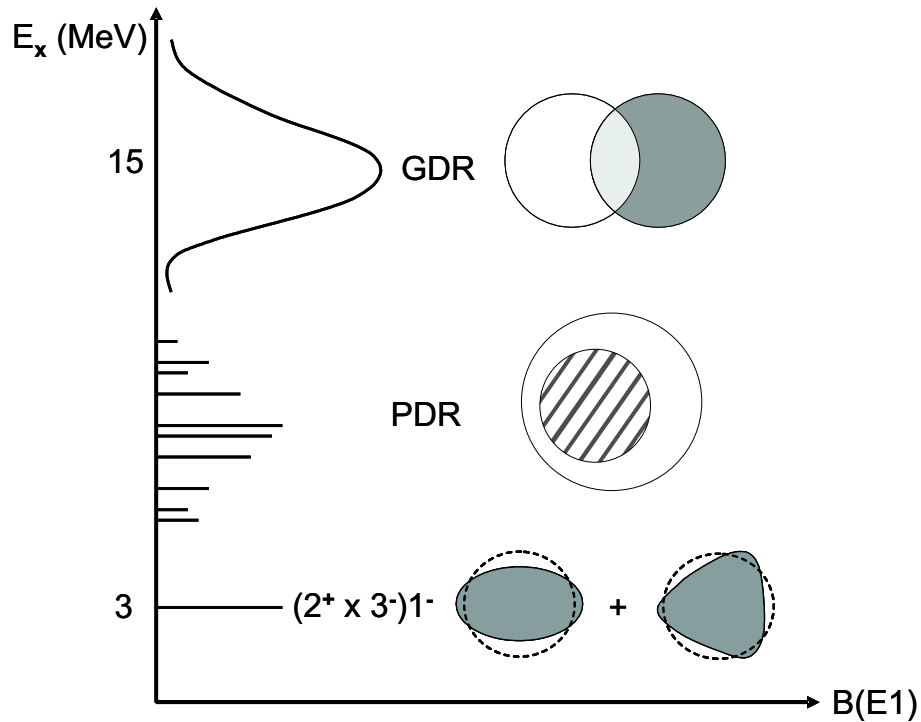
Figure 3.3   Electric dipole excitations in nuclei

The typical example of a collective excitation is the GDR where neutrons and protons vibrate against to each other and it is concentrated at an excitation energy well above 10 MeV. This resonance has been experimentally studied for a long time (Bothe et al., 1937; Baldwin et al., 1947; Baldwin et al., 1948) and explained very well with theoretical models (Migdal,1944; Goldhaber, et al. 1948; Steinwedel et al., 1950). In neutron rich nuclei, it was suggested that another type of resonance might exist the so-called Pygmy Dipole Resonance (PDR), located close to the neutron threshold. It is reflecting the oscillation of the neutron skin against an approximately isospin saturated core. It's nature is completely different from the representation where proton and neutron fluids as whole a move against each other.

In addition one can observe a single strong transition at low energies in spherical nuclei close to the magic proton or neutron shells. This is a two-phonon state which originates from the coupling of quadrupole and octupole phonons. A coupling of these two single phonon excitations leads to a two-phonon quintuplet (Lipas, 1966; Vogel et al., 1971; Grinberg et al., 1994) with spins $J^\pi = 1^-, ..., 5^-$. A schematic representation of the shape vibration and their assumed coupling is displayed in the lower part of the Fig. 3.3.

3.1.2.1 Giant Dipole Resonance

The GDR has been studied most extensively among all the giant resonances because the mode is relatively easy to excite. In photonuclear reactions, i.e., in reactions in which a nucleus is bombarded with energetic gamma rays, total cross sections for GDR excitation are of the order of hundreds of millibarns.

A Lorentzian distribution defines very well the energy dependence of the cross section for an excitation of the GDR in heavy nuclei in photonuclear reactions

$$\sigma_\gamma(E) = \frac{\sigma_{GDR}}{1 + [(E^2 - E_{GDR}^2)^2 / E^2 \Gamma_{GDR}^2]} \tag{3.1}$$

The parameters of this distribution, the resonance energy E_{GDR}, the peak cross section σ_{GDR} at the resonant energy E_{GDR} and the width of the resonance Γ_{GDR}, are functions of the nuclear mass A.

The total cross section for the excitation of the GDR in photonuclear reactions can be compared to the limit given by the so called Thomas-Reiche-Kuhn (TRK) or Energy-Weighted Sum Rule (EWSR)

$$\int_0^\infty \sigma_\gamma dE = \frac{2\pi^2 e^2 h}{mc} \frac{NZ}{A} \approx 60 \frac{NZ}{A} mbMeV \approx 14.9 \frac{NZ}{A} e^2 fm^2 MeV \tag{3.2}$$

where N, Z and A are the neutron, proton and atomic mass numbers respectively.

In medium-mass nuclei the GDR exhausts about 100% of the TRK sum-rule limit. Since the sum rule is proportional to the number of particles in a system, the conclusion can be drawn that all the nucleons take part in the absorption, i.e., that the GDR is a

collective vibration of the whole nucleus.

For heavy nuclei integrals of the experimental photonuclear section exceed the value of the TRK sum rule, which results from exchange and velocity-dependent parts of the nuclear potential omitted in the derivation of the TRK sum rule. In the literature those contributions are usually included via a factor κ, introduced in the following way:

$$\int_0^\infty \sigma_\gamma dE = (1+\kappa)60\frac{NZ}{A}mbMeV \tag{3.3}$$

For $A \geq 90$ nuclei the experimental value of $(1+\kappa)$ varies from about 1 for $A \approx 100$ to 1.3 ± 0.2 for heavy nuclei such as actinide with an average value of 1.2 ± 0.1 (Harakeh, 2001; Adrich, 2005).

3.1.2.2   Pygmy Dipole Resonance

The PDR in neutron-rich nuclei is located usually close to the neutron threshold. Although carrying only a small fraction of the full dipole strength less than 1 % of the EWSR these states are a particular interest because they are reflecting the motion of the neutron skin against an inert core with $N \approx Z$. Here, approximately $N - Z$ neutrons create the neutron skin in nuclei. The skin of the nucleus is also an important subject of current nuclear structure research. There are many different theoretical approaches for the definition of the neutron skin (Krasznahorkay et al., 1991; Myers et al., 1985; Fukunishi et al., 1993; Vretenar et al., 2003).

A wide range of models of the PDR has been discussed ranging from a hydrodynamical description (Mohan et al., 1971; Suzuki et al., 1990), neutron excess surface density oscillations (Chambers et al., 1994, Van Isacker et al., 1992; Adams et al., 1996), fluid-dynamical approaches (Bastrukov et al., 1993; Balbutsev et al., 1994; Misicu et al., 2002), clustering in heavy nuclei (Iachello, 1985) and sum-rule approaches to nonrelativistic and relativistic RPA and QPM calculations. In a macroscopic picture there are different explanations of producing low-lying E1 strength shown in Fig. 3.4. Especially the hydrodynamical model by Mohan, Danos and Biedenhorn (Mohan et al., 1971) describe the PDR mode in nuclei. They use a three-fluid hydrodynamical model of nuclei, the three fluids being the protons, the neutrons of the same orbitals as protons, and the
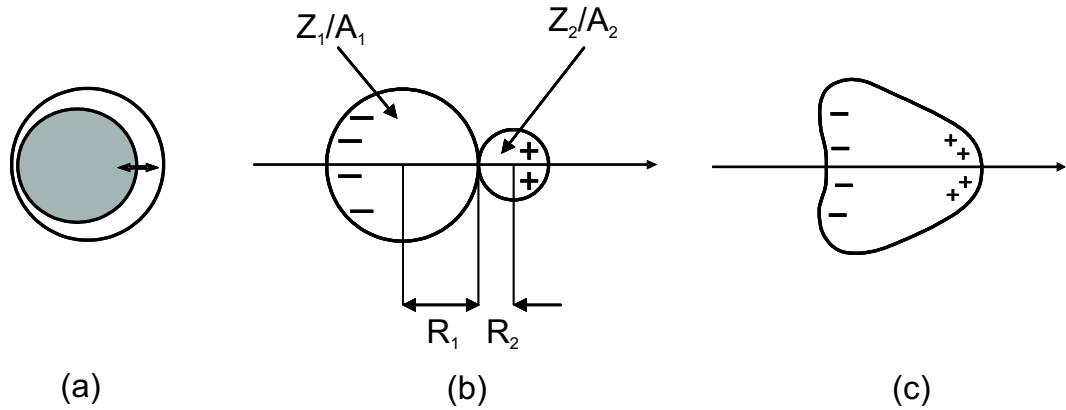
Figure 3.4   Possible configurations with nonuniform proton-neutron distributions.(a) oscillation of excess neutrons against to a proton-neutron core, (b) clustering with different charge to mass ratio (*Z/A*), (c) octupole deformation. The plus and minus signs indicate an increase (+) or decrease (-) of the proton density.

excess neutrons, to account for the fact that the excess neutrons interact less strongly with the protons than do the neutrons which occupy the same space-spin states as the protons (blocked neutrons). According to this model, the reason for considering the nucleus to be made up of three fluids instead of two is the difference in the interaction of the protons with the two kinds of neutrons in different shells. The blocked neutrons interact much more strongly with the protons than the excess neutrons because of the large spatial over-lap of protons and neutrons having the same space-spin quantum numbers. The shape of a possible oscillation is shown in part (a) of Fig. 3.4. Two fluid dynamics, one for excess neutrons and one for the proton-neutron core, has been proposed by Suziki, Ikeda and Sato (Suzuki et al., 1990).

In addition Iachello predicted that two mechanisms produce E1 transitions and local rather than global symmetries are more appropriate to describe both mechanisms (Iachello, 1985). In nuclear physics, one usually analyzes the properties of operators under global isospin transformations. This approach relies on the assumption of a uniform distribution of protons and neutrons. If this is not the case, there are at least two examples of electric dipole modes due to the different charge distribution. These are illustrated in Fig 3.4 (b) and (c). The first example is the case which the nucleus clusterizes into fragments with different charge to mass ratio (*Z/A*) in Fig 3.4 (b). The center of mass does not coincide any more with the center of the charge, producing an electric dipole moment, *D*, of magnitude

$$D = e^2[(N-Z)/A]R_0(A_1^{1/3} + 4^{1/3}) \tag{3.4}$$

for the example of alpha clustering. This dipole moment is not negligible and will produce E1 transitions of considerable magnitude. The second mechanism is shown in part (c) of Fig. 3.4. Consider the case in which the nucleus has a permanent octupole deformation. This produces a dipole moment

$$D = 0.000687AZ\beta_2\beta_3(efm), \tag{3.5}$$

where β_2 and β_3 are the quadrupole and octupole deformations.

For a final understanding we need microscopic models where the low-lying E1 strength occurs naturally. There are different approaches to predict a low-lying E1 resonance in nuclei like microscopic density fluctuation theory (DFT) (Chambers et al., 1994) or describing out-of-phase motion of neutrons against to protons including the effect of neutron thickness (Van Isacker et al., 1992). These models usually overestimate the B(E1) strength and always expect a rather simple direct correlation between the summed strength and the neutron excess. In recent years a number of microscopic approaches like QRPA (Oros et al., 1998; Colò et al., 2000) and relativistic QRPA (Vretenar et al., 2000; 2002; Paar et al., 2005) based on the relativistic Hartree-Bogoliubov model with a density-dependent meson exchange (DD-ME) interaction, the QPM (Ryezayeva et al., 2002) which goes beyond the RPA and includes the coupling to more complex configurations. QPM calculations based on a Woods-Saxon ground state and a separable multipole force for the residual interaction (Tsoneva et al., 2004) and the extended theory of finite fermion systems (ETFFS) (Hartmann et al., 2004) have been used to calculate the PDR. The predictions for the PDR differ substantially, in particular between nonrelativistic and relativistic models.

3.2   Nuclear Resonance Fluorescence (NRF) Method

The nuclear resonance fluorescence method has been proven to be an outstanding tool to investigate low-lying dipole excitations in nuclei and to provide detailed spectroscopic information. It has been used efficiently since the 60's (Metzger, 1959; Kneissl et al., 1996; 2006). In this method monoenergetic electrons are delivered to a radiator target. These produce continuous bremsstrahlung spectra of real photons extending up to the kinetic energy E_0 of the incoming electrons. Bremsstrahlung photons are used to irradiate the target which is made of the isotope to be investigated. A simplified picture of this process is shown in Fig. 3.5. Nuclei of the target material are excited by the photons and emit characteristic gamma rays. The emitted gamma rays are detected with at least two high-purity germanium (HPGe) detectors located at $90°$ and $130°$. These angles are selected to determine the multipolarities of the transitions.

The real photon probe offers particular advantages. The low transfer of momentum of real photons gives rise to a high selectivity in exciting low-spin states (dipole transitions) for J=0 ground state targets. Furthermore, the continuous bremsstrahlung radiation excites simultaneously all states from the ground state. The observables which can be obtained from this pure electromagnetic excitation method are:

- the energy of the state,

- the γ-decay branching ratios to the ground state and particularly to excited states,

- the multipolaritiy of the transition which determines the spin,

- the absolute transition strength or lifetime of the state,

- the parity of the state if one uses either polarized bremsstrahlung in the entrance channel or a Compton polarimeter in the exit channel (this is experimentally possible for even-even nuclei only).

All these observables are deduced from the measured γ-spectra in a totally model independent way which makes real photon scattering a powerful and reliable method (Kneissl et al., 1996).
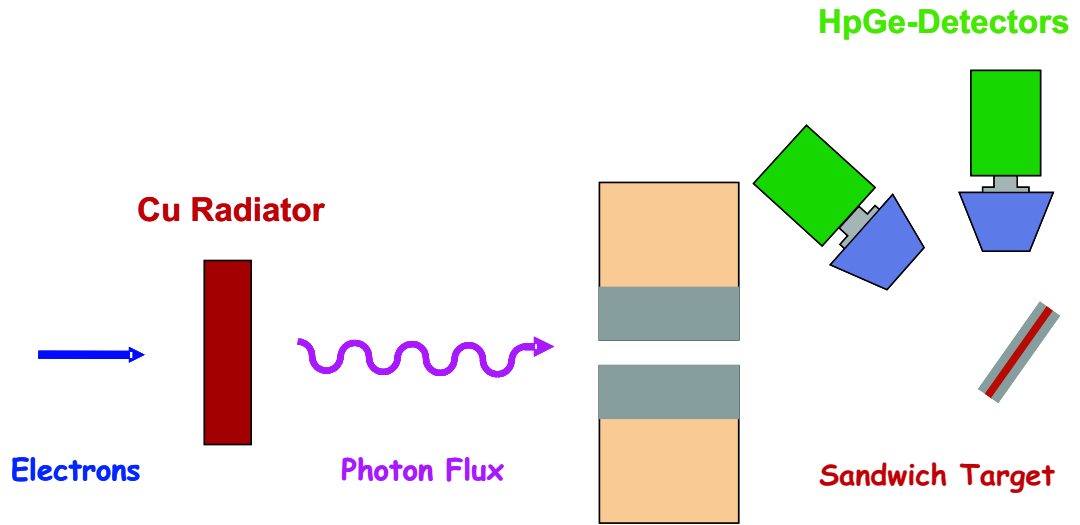
Figure 3.5   The simplified picture of NRF process

The main principle of the NRF method is based on the process of resonant excitation of a nuclear level due to the absorption of a real photon and the subsequent decay of this level by remission of a photon. In this case, the incoming photon excites the target nucleus which has J_0 total angular momentum to a state with total angular momentum J. There is two possible ways to decay from this level; direct decay to the ground state with Γ_0 transition width or to any state between the ground state and the excited level which has J_i total angular momentum with transition width Γ_i. Fig. 3.6 shows this excitation-deexcitation scheme.

The quantities Γ_0, Γ_i and Γ are the transition width to the ground state, to the intermediate level and the total transition width, respectively. The correspondence between the widths is

$$\Gamma = \Gamma_0 + \sum_{i>0} \Gamma_i \tag{3.6}$$

with i being the sum over all intermediate levels. The total decay width is related to the lifetime via the Heisenberg uncertainty relation

$$\tau * \Gamma = \hbar \tag{3.7}$$
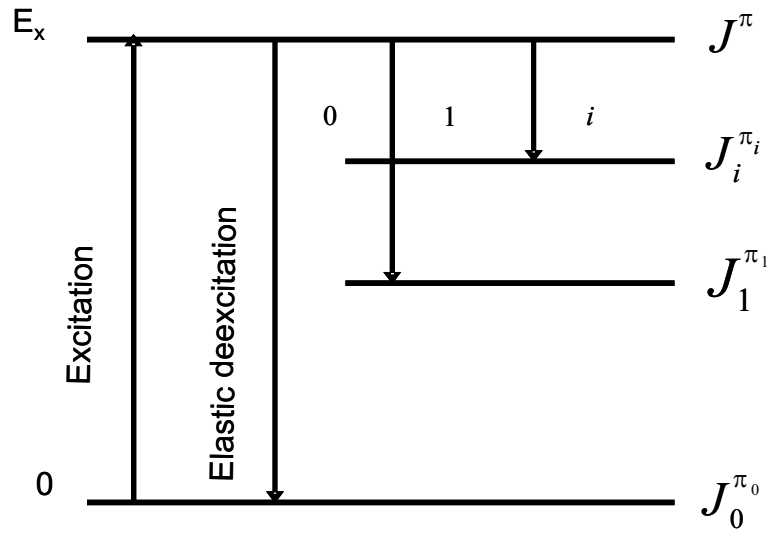
Figure 3.6   The excitation-deexcitation scheme in NRF experiments

The electromagnetic transitions are characterized by the multipolarity λ, where $\lambda=1,2,...$ corresponds to dipole, quadrupole transitions etc. According to selection rules allowed electromagnetic transitions are related to the spins of the initial and final states J_i and J_f by

$$|J_i - J_f| \leq \lambda \leq J_i + J_f. \tag{3.8}$$

The parities of these states define the type of the transition:

$\pi_i = (-1)^{\lambda} \cdot \pi_f$ for electric transitions, $\pi_i = (-1)^{\lambda+1} \cdot \pi_f$ for magnetic transitions.

3.2.1   Integrated Cross Section

The cross section for the process of a nuclear transition from the ground state through an excited state to a final state with J_i total angular momentum is described by the Breit-Wigner formula

$$\sigma_i = \frac{\pi}{2} \left(\frac{\hbar c}{E_{x_i}} \right)^3 \cdot g \cdot \frac{\Gamma_0 \Gamma_i}{(E_\gamma - E_{x_i})^2 + \frac{\Gamma^2}{4}}, \tag{3.9}$$

where E_γ is the energy of incoming photon, E_{x_i} is the excitation energy of level i and g is a statistical factor which depends on the total angular momentum of the ground state J_0

and the angular momentum of the excited level J

$$g = \frac{2J + 1}{2J_0 + 1}.$$ (3.10)

The total cross section is given by the sum of partial cross sections of the decays all possible final states.

$$\sigma_{abs}^{total} = \sum_i \sigma_{abs}^i (E_\gamma) = \sum_i \frac{\pi}{2} \left(\frac{\hbar c}{E_{x_i}} \right)^3 \cdot g \cdot \frac{\Gamma_0 \Gamma_i}{(E_\gamma - E_{x_i})^2 + \frac{\Gamma^2}{4}}.$$ (3.11)

When a nucleus which is initially at rest and in a ground state absorbs a primary γ quantum with the energy E_γ, a part of the energy ΔE_{rec} is transferred to the nucleus as a recoil because of the finite mass of the nucleus. The relation between the recoil energy and E_γ is $E_\gamma = E_x + \Delta E_{rec}$, with

$$\Delta E_{rec} = \frac{E_\gamma^2}{2Mc^2},$$ (3.12)

where M is the rest mass of the nucleus. The excited nucleus is not at rest any more, but it is moving in the direction of primary photon beam. If during the short decay time to the ground state a secondary photon is emitted, its energy will experience a Doppler shift in addition to the recoil correction. Thus, the emitted photon will have a different energy dependence on the emission angle θ with respect to the incoming γ-quantum, which excites the nucleus

$$E_\gamma = E_x - \frac{E_\gamma^2}{2Mc^2} [1 - 2\cos\theta].$$ (3.13)

If this energy is large compared to the width of the level, as is generally the case, then the cross section for resonance absorption of the emitted photon by some another neighboring nucleus becomes extremely small. This is a precondition to make the detection of emitted photons with the NRF method possible at all.

Another important factor for NRF experiments which should be taken into account in this formula is the thermal motion of atoms in the target. This motion causes a Doppler

broadening of the absorption line width. If we assume that the thermal velocities of nuclei v can be given as a Maxwell distribution (Bethe et al., 1937)

$$f(v) = \left(\frac{M}{2\pi kT}\right)^{1/2} exp\left(-\frac{Mv^2}{2kT}\right),$$

(3.14)

where M is the nuclear mass, k is the Boltzmann constant, and T the absolute temperature, then the Doppler-broadened Breit-Wigner distribution

$$\sigma_{DBW}^{i}(E_\gamma, T) = 2\pi \left(\frac{\hbar c}{E_x}\right)^2 \cdot g \cdot \frac{\Gamma_0}{\Gamma} \cdot \frac{\Gamma_i \sqrt{\pi}}{2\Delta} exp\left(-\frac{E_\gamma - E_x}{\Delta}\right)^2,$$

(3.15)

replaces Eq. (3.9). Here, Δ is the Doppler width

$$\Delta = \left(\frac{E_\gamma}{c}\right) \cdot \left(\frac{2kT}{M}\right)^{1/2}.$$

(3.16)

We can use this Doppler-broadened distribution to extract the partial cross section I_i for the population of level by integration of Eq. (3.15). over the complete solid angle

$$I_i = \int \sigma_{DBW}^{i}(E_\gamma, T) dE_\gamma = \pi^2 \cdot \left(\frac{\hbar c}{E_x}\right) \cdot g \cdot \frac{\Gamma_0 \Gamma_i}{\Gamma}.$$

(3.17)

In case of the elastic transition Γ_0 will be equal to Γ_i and Eq. (3.17) replace to

$$I_0 = \pi^2 \cdot \left(\frac{\hbar c}{E_x}\right) \cdot g \cdot \frac{\Gamma_0^2}{\Gamma}.$$

(3.18)

3.2.2   Transition Width and Transition Strength

The ground state decay width is proportional to the reduced transition probability $B(\Pi\lambda, E_\gamma)$

$$\Gamma_0 = 8\pi \sum_{\Pi\lambda=1}^{\infty} \frac{\lambda+1}{\lambda[(2\lambda+1)!!]^2} \cdot \left(\frac{E_\gamma}{\hbar c}\right)^{2\lambda+1} \cdot \frac{2J_0+1}{2J+1} B(\Pi\lambda, E_\gamma) \uparrow,$$

(3.19)

where $\Pi = E$ for electric transitions and $\Pi = M$ for magnetic transitions. The NRF technique is selective on dipole transitions and to a lesser extent on quadrupole transitions because of the small momentum transfer of the photons. The relations between reduced transition strengths and ground state decay width are given for even-even nuclei in the following

$$\frac{B(E1)\uparrow}{[e^2 fm^2]} = 9.554 \cdot 10^{-4} \cdot g \cdot \frac{\Gamma_0}{[meV]} \cdot \left(\frac{MeV}{E_x}\right)^3, \tag{3.20}$$

$$\frac{B(M1)\uparrow}{[\mu_N^2]} = 8.641 \cdot 10^{-2} \cdot g \cdot \frac{\Gamma_0}{[meV]} \cdot \left(\frac{MeV}{E_x}\right)^3, \tag{3.21}$$

$$\frac{B(E2)\uparrow}{[e^2 fm^4]} = 1.245 \cdot 10^3 \cdot g \cdot \frac{\Gamma_0}{[meV]} \cdot \left(\frac{MeV}{E_x}\right)^5. \tag{3.22}$$

The reduced transition probabilities for the decay $B(\Pi\lambda; J \to J_0) = B(\Pi\lambda)\downarrow$ and $B(\Pi\lambda; J_0 \to J) = B(\Pi\lambda)\uparrow$ differ by the statistical factor introduced in Eq. (3.10)

$$B(\Pi\lambda)\uparrow = \frac{2J+1}{2J_0+1} \cdot B(\Pi\lambda)\downarrow. \tag{3.23}$$

It is useful to compare the reduced transition strength to the so-called Weisskopf units, which represent a measure of the single-particle strength. It is given for electric transitions by

$$B(E\lambda)_{W.u.} = B(E\lambda)\downarrow = \frac{1}{4\pi}\left[\frac{3}{\lambda+3}\right]^2 (1.2A^{1/3})^{2\lambda} e^2 fm^{2\lambda}. \tag{3.24}$$

3.2.3   Angular Distribution

The spins of the excited levels can be determined by measuring the angular distributions of the scattered photons with respect to the incoming photon beam. The general

formula for the angular correlation function $W(\theta)$ of the scattered photon can be given as a sum of even Legendre polynomials $P_\lambda(\Theta)$:

$$W(\theta) = \sum_{\lambda=0,2,4,\ldots} A_\lambda^{i \to j} \cdot A_\lambda^{j \to k} \cdot P_\lambda(cos\theta), \qquad (3.25)$$

where θ is the scattering angle between the direction of incident photon and the scattered photon and $P_\lambda(cos\theta)$ are Legendre polynomials of order λ. The coefficient $A_\lambda^{i \to j}$ describes the photon in the entrance channel, and similarly $A_\lambda^{j \to k}$ takes into account the resonantly scattered photon.

Even-even nuclei always have ground state angular momentum and the parity $J_0^\pi = 0^+$. As a consequence, only levels with 1 or 2 can be excited in (γ, γ') experiments on even-even targets. The angular distribution of photons scattered of even-even nucleus with ground state spin 0, representing the most favorable case, through a pure dipole transition (spin sequence 0-1-0) is given by

$$W(\theta)_{dipole} = \frac{3}{4} \cdot (1 + cos^2\theta) \qquad (3.26)$$

and through a pure quadrupole transition (spin sequence 0-2-0) is given by

$$W(\theta)_{quadrupole} = \frac{5}{4} \cdot (1 - 3cos^2\theta + 4cos^4\theta) \qquad (3.27)$$

These angular distributions are depicted as polar diagrams in Fig. 3.7. It is evident that for spin assignments in even even nuclei at least two different angles is need to be measured. The most favorable configuration is $\theta = 90°$ and $\theta = 127°$. In the case of even-even nuclei the predicted values for the ratio of measured γ intensities at $90°$ and $127°$

$$\frac{W(90°)_{0 \to 1 \to 0}}{W(127°)_{0 \to 1 \to 0}} = 0.73 \qquad (3.28)$$

$$\frac{W(90°)_{0\to2\to0}}{W(127°)_{0\to2\to0}} = 2.28 \tag{3.29}$$

These values are slightly reduced for realistic geometries used in the experiments due to the finite solid angles of the detectors. Unfortunately, in the case of odd-A nuclei the angular distributions are, due to the half-integer spins involved in the cascades, nearly isotropic. Therefore, it is difficult to extract conclusive information on the spins of the excited levels. This can be achieved in typical NRF set-ups in only a few favorable cases (e.g., $J_0 = 1/2$) (Geiger et al., 1994). As can be seen in Fig. 3.7, at 90° the angular distribution for dipole transitions has a minimum, whereas for quadrupole transitions it has a maximum at 90° and two minima at 53° and 127°. The angle θ= 127° is more favorable than θ= 53° because of the dramatic background decrease at backward angles. Therefore the detectors are placed at these angles and comparing the intensities of lines one can distinguish between quadrupole and dipole transitions.
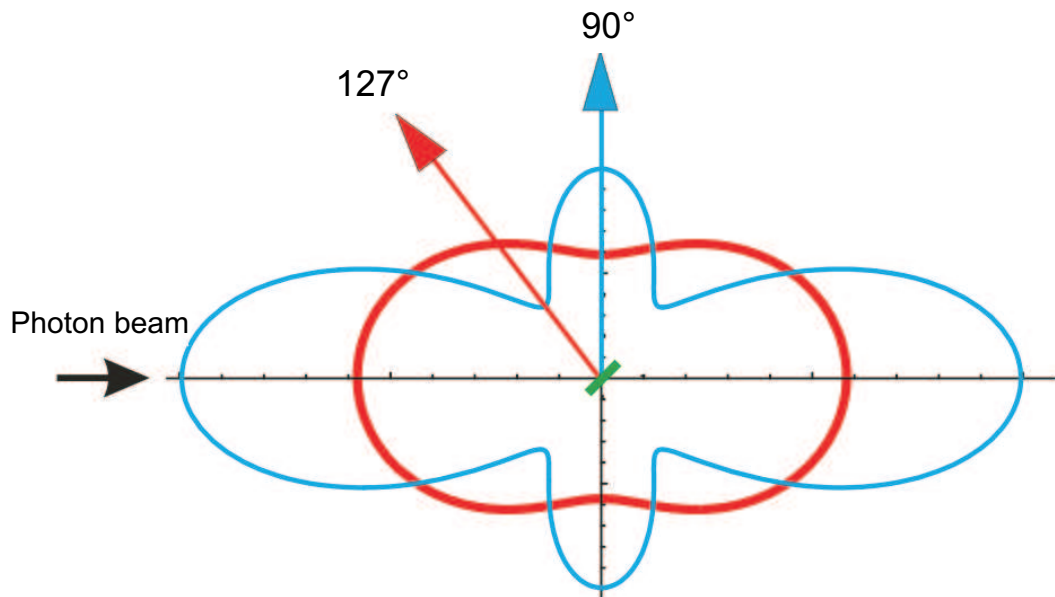
Figure 3.7   Angular distribution patterns for scattered photons of even-even nuclei for pure dipole (0-1-0) and quadrupole (0-2-0) cascades

3.3   Photon Scattering Experiments at the S-DALINAC

3.3.1   The S-DALINAC

The present (γ,γ') experiments ware performed at the superconducting Darmstadt electron linear accelerator S-DALINAC (Richter, 1996). The S-DALINAC is historically the third superconducting electron linac. It produced its first beam (Auerhammer et al., 1992) in 1987 and went into full operation (Auerhammer et al. 1993; Aab et al., 1988) in 1991. The layout of the superconducting recirculating electron accelerator S-DALINAC is shown in Fig. 3.8.
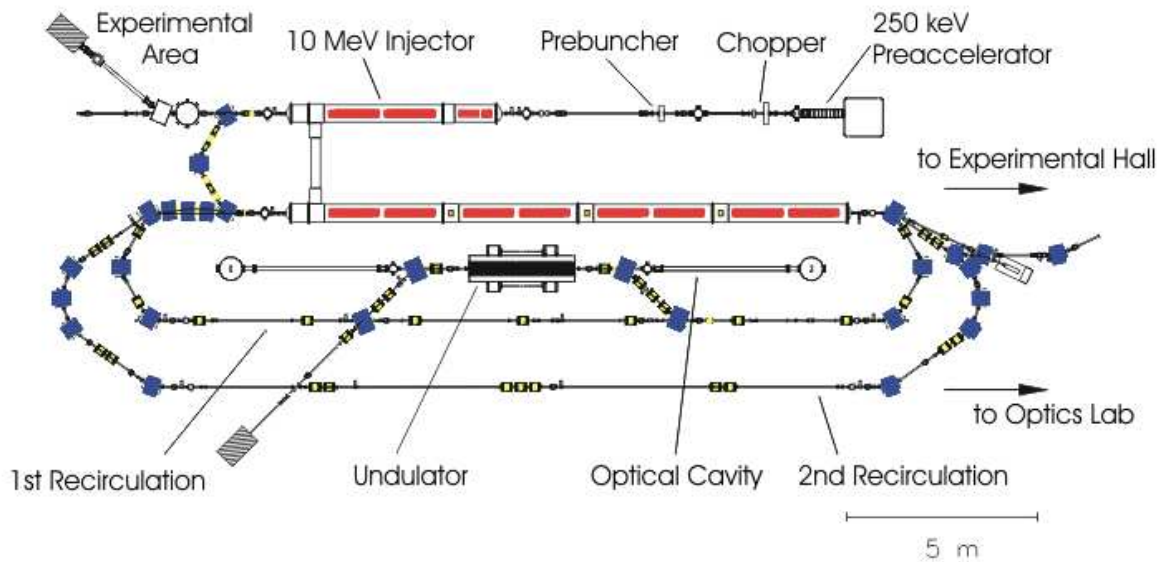
Figure 3.8   Schematic layout of the S-DALINAC

The electron source is located on a high voltage terminal (top right) at 250 keV. The electrostatically preaccelerated beam gets its time structure (necessary for succesive acceleration in the superconducting rf cavities at 3 GHz) in the chopper-prebuncher section at room temperature, where the DC current from the source is first chopped into 30 ps long packages which are then bunched to a length of 5 ps when they enter the superconducting injector linac. Acceleration is then achieved by a 2-cell capture cavity (β=0.85) followed by a 5-cell capture cavity (β=1) and two 20-cell accelerating cavities, all fab-

ricated from RRR=280 niobium and operated in liquid helium at 2 K. When leaving the injector, the beam has an energy of up to 10 MeV and can either be used for low energy experiments (the photon scattering) or it can be bent isochronously by $180°$ for injection into the main linac. There, eight 20-cell cavities installed in four identical cryomodules increase the beam energy by up to 40 MeV. One of the superconducting 20-cell cavities of the S-DALINAC is displayed in Fig 3.9 and the most important parameters are shown in Table 3.1, where E_{acc} is electric field strength, $Q_{/circ}$ is quality factor and P_{dis} is dissipated power.
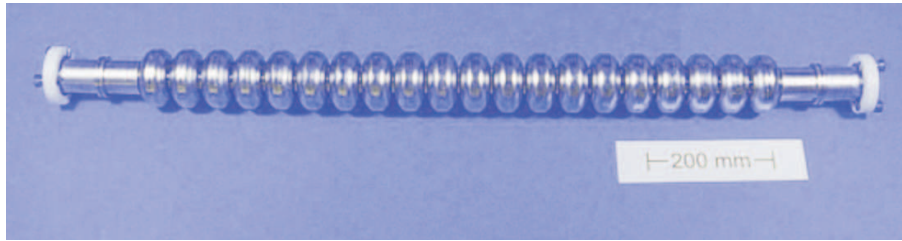
Figure 3.9   20-cell 3 GHz superconducting cavity.

Table 3.1   Important parameters of 20-cell superconducting cavity.

Material	: Nb	$\prod$	- Mod
Length	: 1 m	E_{acc}	= 5 MV/m
Frequency	: 3 GHz	$Q_{/circ}$	$= 3 * 10^9$
Temperature	: 2 K	P_{dis}	= 4 W

When leaving the main linac the beam can either be extracted to the experimental hall or it can be recirculated and reinjected one or two times by the appropriate beam transport systems (lower part of Fig. 3.8). The maximum beam energy after three passes through the main linac therefore amounts to 130 MeV delivered to different experimental facilities shown schematically in Fig. 3.10.

A wide range of electron scattering experiments is carried out using the large solid angle and momentum acceptance magnetic spectrometer QCLAM or magnetic spectrometer Lintott, optimized for beam dispersion matching to obtain the highest possible resolution.

Accelerator Hall | Experimental Hall

① ③

② ⑤ ④ ⑥

0   5m

① Real Photon (γ,γ') ⑤ (e,e')-Experiment
② Free-Electron-Laser   ⑥ Compton scattering
③ High energie-beam physics   of the nucleon
④ (e,e'x)-Experiment & 180°-Spectrometer   ⑦ Laser-Experiment
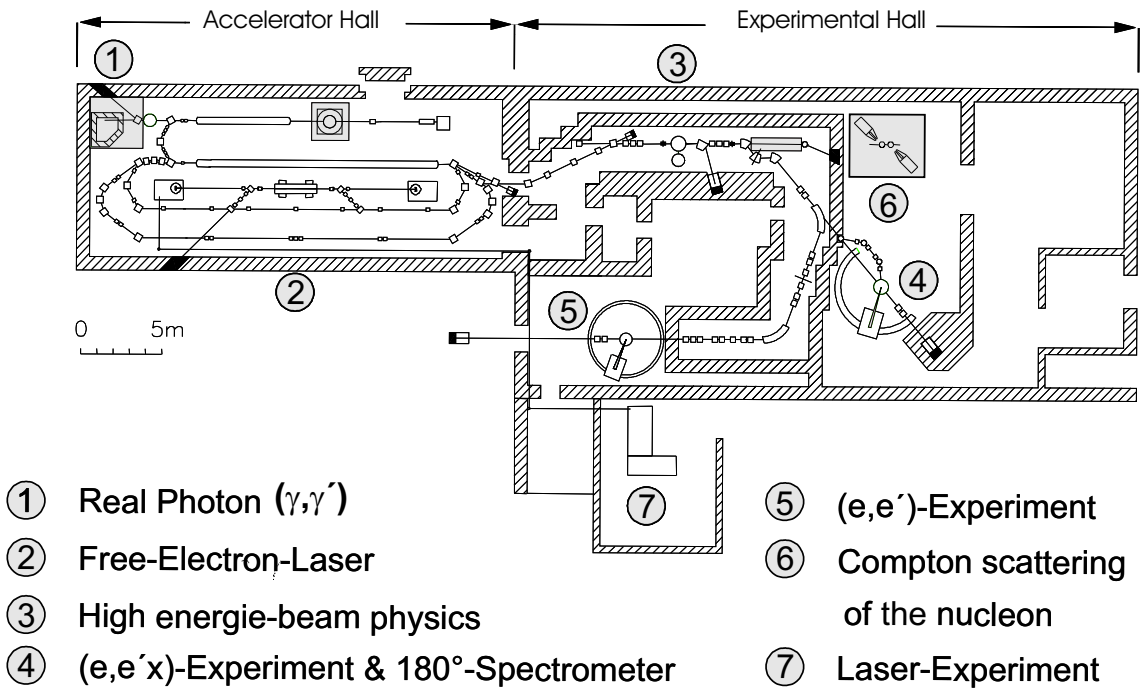
Figure 3.10   Experimental facilities at the S-DALINAC.

3.3.2 NRF Setup

The NRF setup (Mohr, et al., 1999) at the S-DALINAC is located immediately behind the injector indicated in Fig. 3.10 as section 1. A schematic layout of the NRF setup is presented in Fig. 3.11. The monoenergetic electron beam with energies up to 10 MeV and currents of typically $30-50\mu A$ is stopped in a 1.5 cm thick rotating and air-cooled copper radiator target. Copper is chosen to avoid background resulting from (γ, n) spectra and subsequent (n, γ) capture in the surrounding and detector materials. Between the bremsstrahlung source and the scattering probe a 95.5 cm thick copper collimator is installed to cut out the central part of the bremsstrahlung cone. The neutron separation energies $S_n = 9.91$ MeV and $S_n = 10.9$ MeV of the two exist stable isotopes ^{63}Cu and ^{65}Cu, respectively, allow for electron energies up to 10 MeV. The collimator was made of copper bricks with dimensions $300 \times 300 \times 100$ mm^3 and a weight of about 70 kg which are available
commercially. The collimator hole in the center of each brick has a conical shape, starting with a diameter of $d_1 = 12$ mm in the first brick on the side of the bremsstrahlung target and ending with $d_2 = 20$ mm in the last brick on the side of the photon target. Addi-
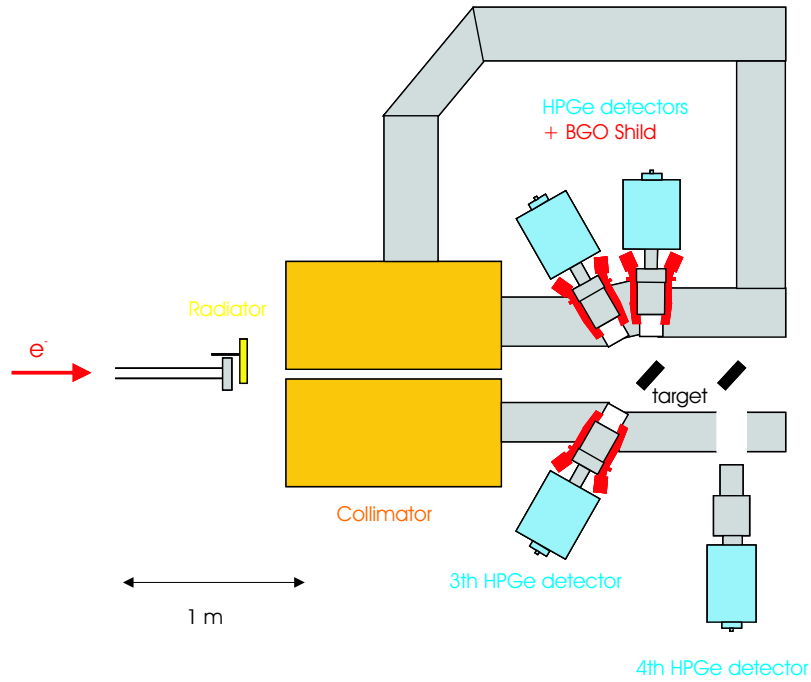
Figure 3.11   Schematic layout of the NRF setup at the S-DALINAC

tional copper bricks are arranged around the collimator on the radiator side. Because the bremsstrahlung is emitted mainly in forward direction, this setup avoids neutron-induced background from the collimator.

Four detectors are located at different angles to determine the multipolarities and parities of the transition. These are described in the next section.

3.3.3   Detectors

Germanium detectors are the most preferred detectors for gamma-ray spectroscopy. High purity germanium (HPGe) detectors with a density of impurities of less than 10^{10} atoms/cm^3 were used in the present experiments. They can supply high energy resolution of a few keV for energie up to 10 MeV. The HPGe crystal purity is not affected by temperature, allowing storage without cooling, but due to the small band gap of germanium (0.7 eV) they must be cooled to liquid nitrogen temperature (77 K) in order to reduce thermal noise during operation. For gamma-ray spectroscopy an active volume as large as possible is required, so detectors are constructed with a coaxial shape which is shown in Fig. 3.12. A part of the central core is removed from the crystal and the electrical

contacts are attached at the center and the outside of the crystal. In a n-type detector the inner contact is a thick n-dopped 600 mm thick and the outer contact a thin p-dopped 0.3 mm thick (the n, p convention refers to acceptor and donor doping material). This is a usual arrangement for gamma ray spectroscopy since the thick n+ contact would produce greater attenuation at the outside edge.
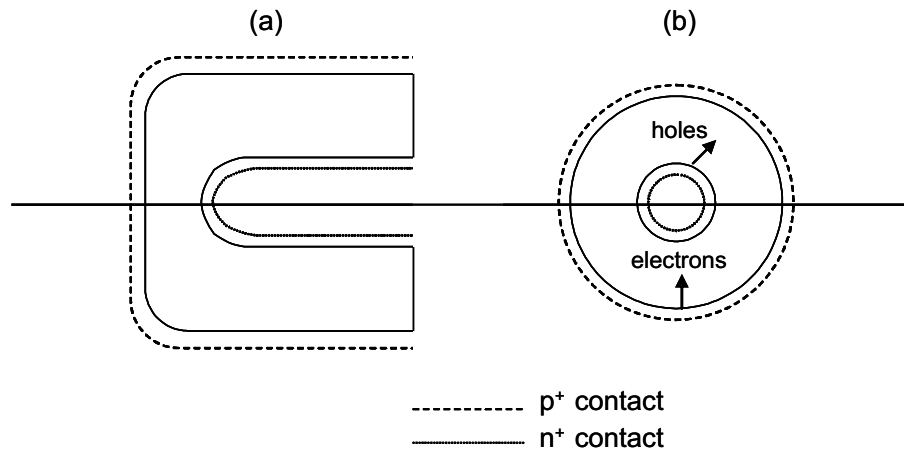
 Figure 3.12   Scheme of a n-type coaxial HPGe detector: (a) perpendicular view and (b) is through the axis of the crystal

When a γ ray enters such a detector, it must produce at least one recoil electron by one of three processes photoelectric effect, the Compton effect, or pair production before it is recorded as an event.

In the photoelectric process, the γ ray gives all of its energy to the recoil electron. The recoil electron then produces electron-hole pairs in the detector that yield the output pulse. For the photoelectric process, the output pulse from the detector is proportional to the energy of the γ ray that produced the interaction. In the spectrum, these events will show up as full-energy photopeaks.

In the Compton process, there is a distribution of pulse amplitudes up to some maximum pulse height. This maximum pulse height produces the Compton edge and there is a statistical probability that each event can produce a pulse with any height up to this maximum with about equal chance. Thus, Compton events will provide a distributed low-energy area in the spectrum. In modern, large detectors with high peak-to-Compton ratios, some Compton events also contribute to the full energy peak when the scattered photons undergo one or more additional interactions. This results in complete absorption.

The pair-production process can also provide a total absorption of the γ-ray energy. The gamma enters the detector and creates an electron-positron pair. From the law of conservation of mass and energy, it follows that the initial gamma must have an energy of at least 1.022 MeV because it takes that much energy to create both the negative and positive electrons with energy 0.511 MeV.

For the detection of emitted gammas, three HPGe detectors were used in the present experiments located at 90°, 130° (a little bit shifted from 127°) and -130° according to incoming photon beam. These detectors are positioned approximately 26 cm from the target. The forth detector is the segmented HPGe detector located at 90° for measurements with a second target to determine the parity of transitions via the Compton effect. This detector was not used for the present experiments because parity determination with this type of method needs extremely high statistics which could not be reached with the available beam time.

Furthermore 25 mm lead and 30 mm copper were placed as filters between the target the and detectors to reduce the number of photons from the target impinging on the detectors. Without these filters NRF measurements would not be possible at the typical photon fluxes because of a 10 kHz upper limit on the detectors single count rates. Because of the energy-dependent absorption probability of photons, these filters mainly reduce the low-energy part of the spectrum, where nonresonant process dominate, but hardly reduce the flux in the energy region of interest.

At γ-energies higher than 3 MeV, the pair-production process is the most important gamma interaction. As discussed before, when an incident gamma with sufficient energy enters the crystal, it can create an electron-positron pair. When the positron annihilates, two gammas with equal energy 0.511 MeV are produced and these leave with an angular separation of approximately 180°. These two gammas are indicated as γ_1 and γ_2 in Fig. 3.13. For small detectors, it is very probable that both γ_1 and γ_2 will escape from the detector before they make any further interactions in the crystal. The energy thus absorbed would be E - 1.02 MeV and shows up as a double-escape (DE) peak in the spectrum. As the detector size is increased, the probability becomes larger that either γ_1 or γ_2 will make a photoelectric interaction within the crystal. If one of these gammas makes a photoelectric interaction, the energy of the event that is recorded is the single-escape (SE)

Ge Detector

e^-

Pair production

Incident gamma

γ

e^+

γ_1 γ_2

Annihilation

$\gamma_1 = \gamma_2 = 511$ keV
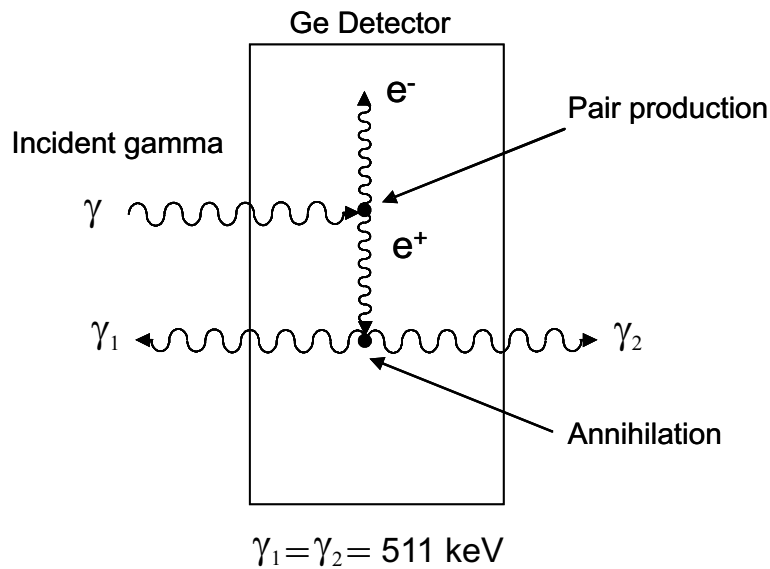
Figure 3.13   Principle of SE and DE.

peak. For even larger detectors, the probability of photoelectric interactions is further increased and both γ_1 and γ_2 could make photoelectric interactions within the crystal. If both γ_1 and γ_2 make photoelectric interactions, the total energy of the incident gamma is absorbed within the crystal.

3.3.4   BGO Suppression

Although these HPGe detectors provide very good resolution in γ-ray spectroscopy, a major experimental problem remains; namely, that of a poor peak-to-background ratio caused by incomplete energy collection in the Ge detector. This problem is common to all experiments using bare Ge detectors. An improvement is achieved by the detection of the scattered radiation in a surrounding detector (an escape suppression shield) and the rejection of coincident events between the Ge detector and the shield. The combination of Ge detector and shield is termed an escape suppressed spectrometer (ESS). A schematic diagram of a modern ESS is shown in Fig. 3.14. Because of its high stopping power, Bismuth Germanate, $Bi_4Ge_3O_{12}$ (BGO) is usually chosen for the surrounding material. This allows suppression shields to be more compact and hence more ESSs can be arranged around a target. After suppression, the peak-to-total ratio is improving distinctly (Beausang et al., 1995). Besides Compton-scattered γ-quanta also events from cosmic rays
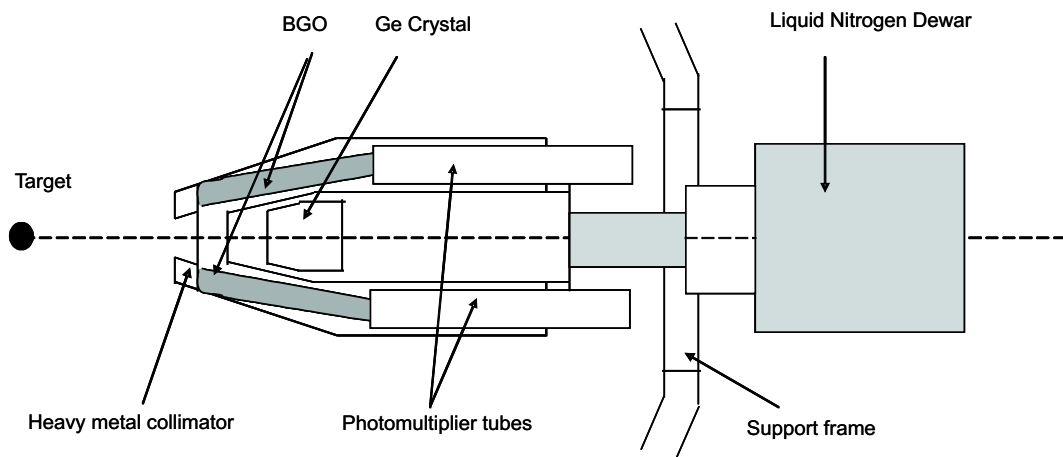
Figure 3.14   Typical construction of HPGe detector with BGO shield
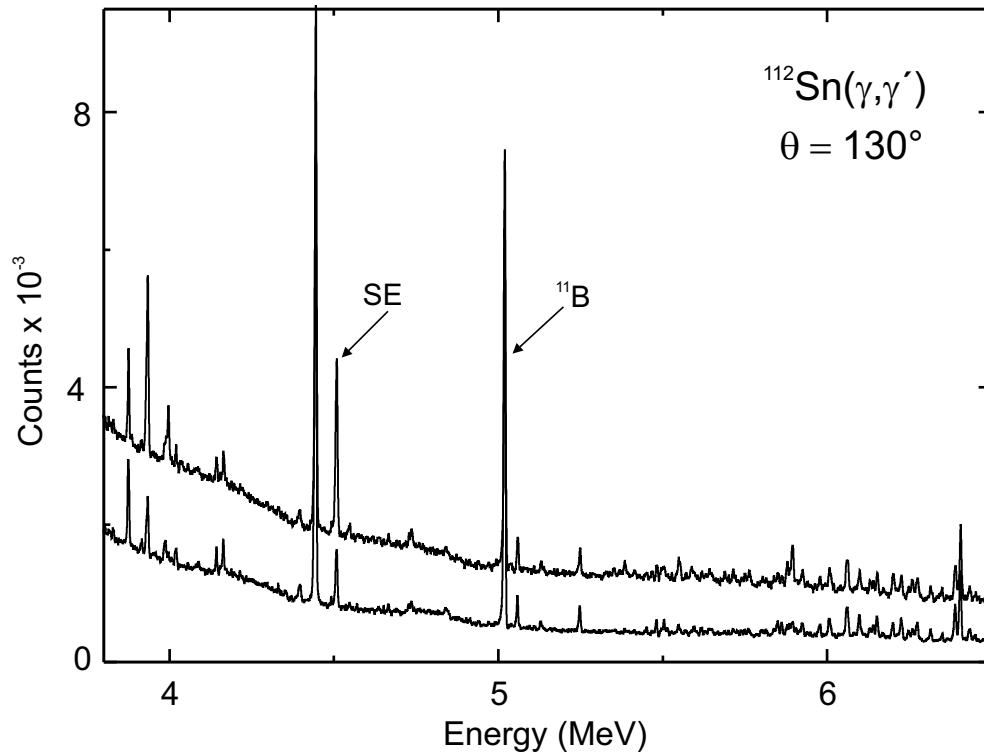
Figure 3.15   Measured spectra with BGO and without BGO

contribute to the background in the spectrum. These events can also be suppressed by the BGO shield. Moreover one can reduce significantly the SE and DE lines. The improvement in the spectrum quality obtained by using of an ESS is demonstrated in Fig 3.15. The figure shows the difference between the spectra which are taken with and without a BGO shield. The background and the SE peak at 4.5 MeV from the strong line of ^{11}B at 5 MeV are distinctly reduced and the DE peak is completely suppressed by using the BGO shield.

4. ANALYSIS and RESULTS

4.1   Analysis of Resolved Transitions

4.1.1   Experimental Details

The NRF experiment for ^{112}Sn was performed in the spring of 2003. Endpoint energies of 5.5 MeV, 7.0 MeV and 9.5 MeV were used to generate bremsstrahlung spectra. The maximum endpoint energy was selected according to the neutron separation energy of 10.790 MeV and the proton separation energy is 7.055 MeV for ^{112}Sn. In the present work the data for 9.5 MeV endpoint energy have been analyzed. The data up to 5.5 MeV and 7.0 MeV have been already analyzed (Poltoratska, 2005) and these results have been used to determine the feeding effect on spectra with 9.5 MeV endpoint energy. The energy-calibrated (γ,γ') spectra of ^{112}Sn up to 9.5 MeV at 90° (upper part) and 130° (lower part) are displayed in Fig. 4.1.
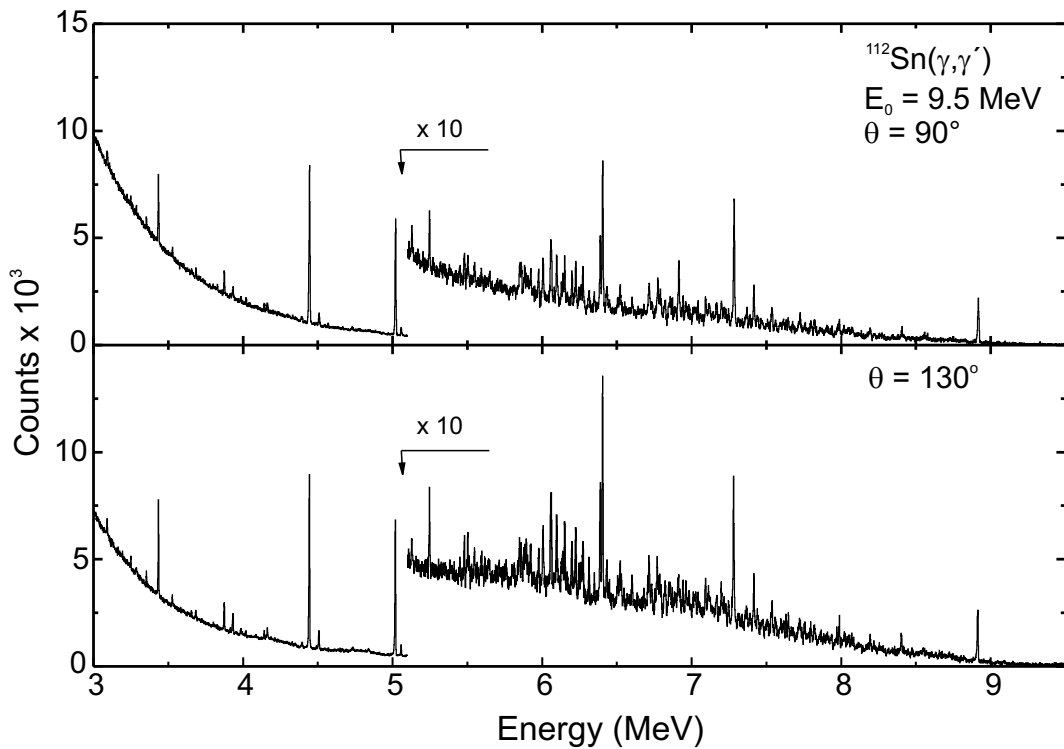
Figure 4.1   Measured spectra for ^{112}Sn up to 9.5 MeV at 90° and 130°
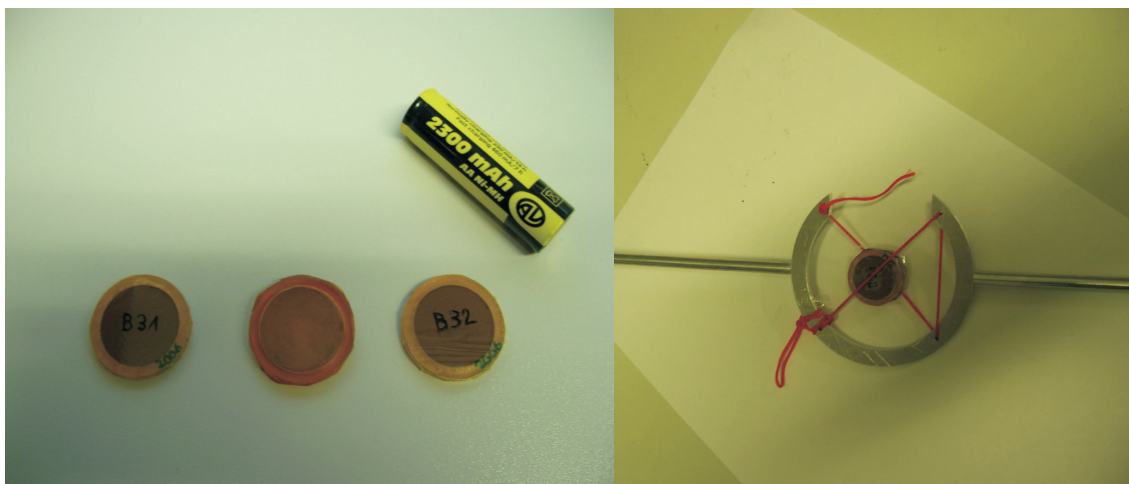
Figure 4.2   One example of a tin target together with two ^{11}B targets)

The target was made of highly enriched (99 %) ^{112}Sn material having a weight of 1990.5 mg, sandwiched between two layers of ^{11}B with a total weight 1017.15 mg. The well known ^{11}B transitions were used to calibrate the spectra and to determine the photon flux. Fig. 4.2 shows an example of a typical target (middle of the left hand side) sandwiched between two layers of ^{11}B and fixed on the target frame (right hand side). The total measurement time at 9.5 MeV was 72 hours using an average electron beam current of 20 μA.

The experiment for ^{120}Sn was performed in spring of 2006. Endpoint energies of 7.5 MeV and 9.1 MeV were used to generate bremsstrahlung spectra. Both data have been analyzed in this work. The neutron separation energy is 9.107 MeV and the proton separation energy is 10.690 MeV for ^{120}Sn. The target made of highly enriched ^{120}Sn had a weight of 1990.2 mg and the ^{11}B layers a total weight of 1288.95 mg. The measurement times were 35 hours at 7.5 MeV and 100 hours at 9.1 MeV using an average electron beam current of 30 μA. The measured spectra of ^{120}Sn with 7.5 MeV endpoint energy in Fig. 4.3 and with 9.1 MeV endpoint energy in Fig. 4.4. are displayed at 90° and 130°. Counts are multiplied by a factor of 10 for energies higher than 5 MeV for better visibility. The experimental energy resolution is starting with 4 keV up to a maximum of 10 keV at the highest energy in all measured spectra.

Well known transitions in ^{11}B (see Table 4.1.) were used for an energy calibration of the measured spectra and determination of the absolute value of photon flux.
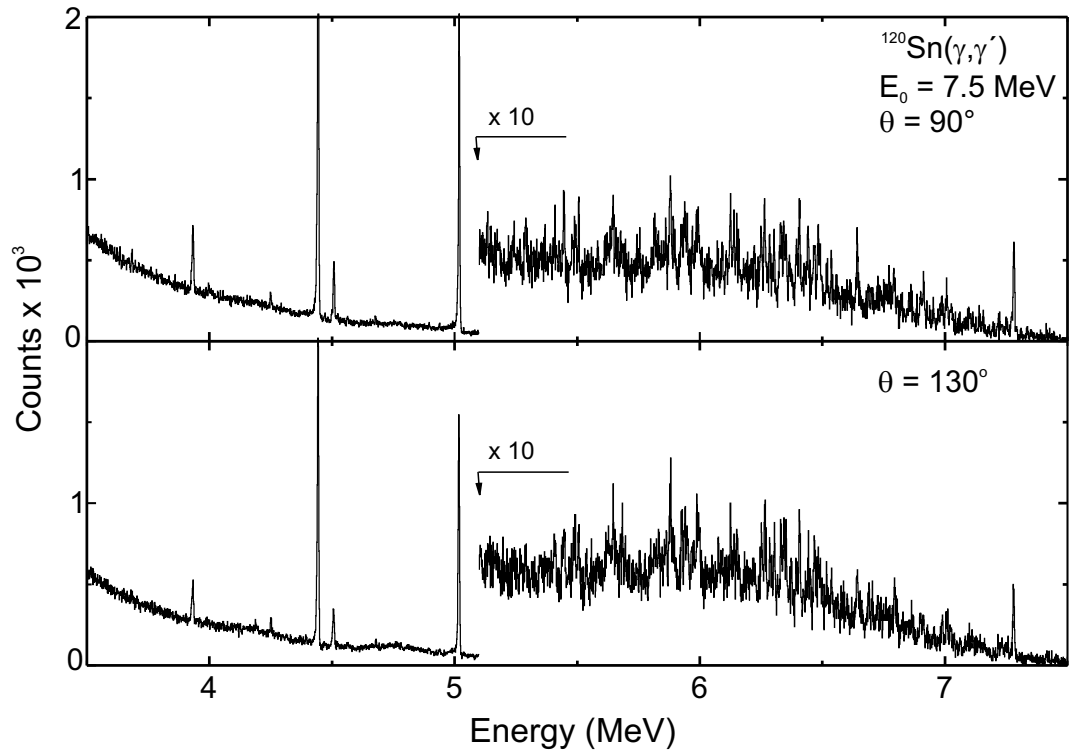
Figure 4.3   Measured spectra for ^{112}Sn up to 7.5 MeV at 90° and 130°
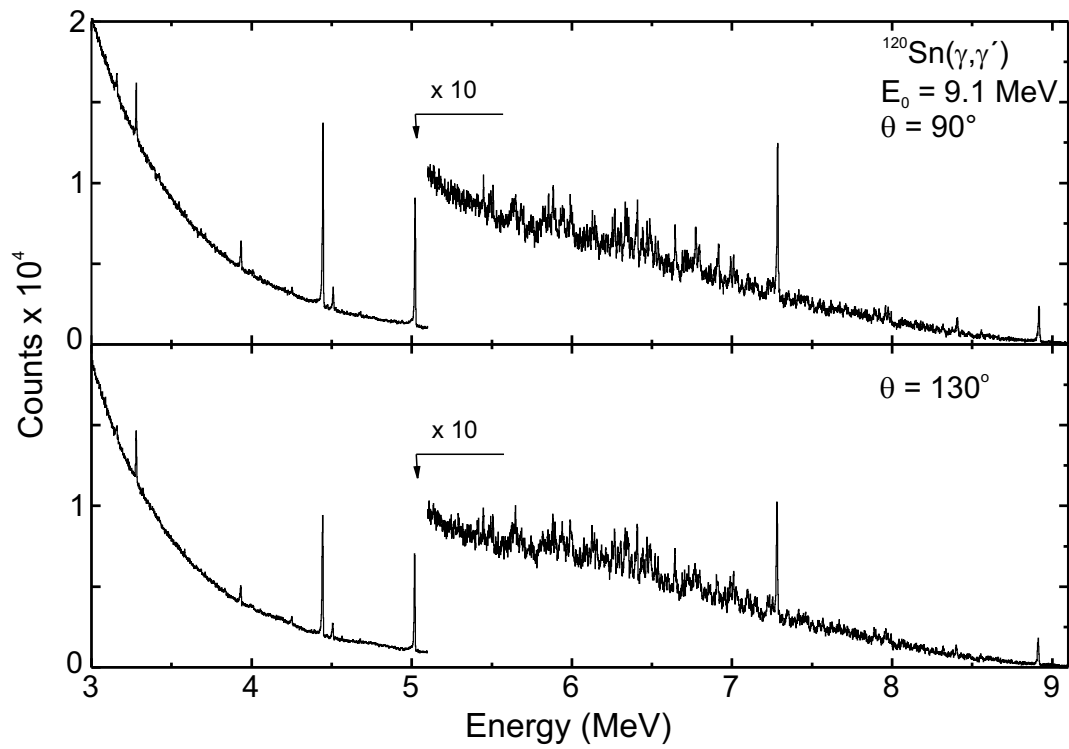
Figure 4.4   Measured spectra for ^{120}Sn up to 9.1 MeV at 90° and 130°

4.1.2   Detector Efficiency

For the extraction of the cross section one has to determine the absolute efficiency of the detectors defined as

$$\varepsilon_{abs} = \frac{number\ of\ detected\ events\ in\ the\ photopeak}{number\ of\ quanta\ emitted\ by\ source}. \tag{4.1}$$

To determine the absolute detector efficiency different sources with known activity should be measured with the same setup and placed exactly at the target position. ^{56}Co and ^{60}Co sources were used in the present measurements. The ^{56}Co radioactive source provides 19 gamma transitions with known relative gamma intensities (NNDC, 2007). Since the maximum energy of known transitions in ^{56}Co reaches to 3.6 MeV only, GEANT4 simulation (Volz, private com.) and a fit function derived from the GEANT4 simulations are used for the higher energy region. Figure 4.5 shows the measured values of ^{56}Co normalized to the GEANT4 simulation for the absolute efficiency of the detectors at $130°$ and $90°$.
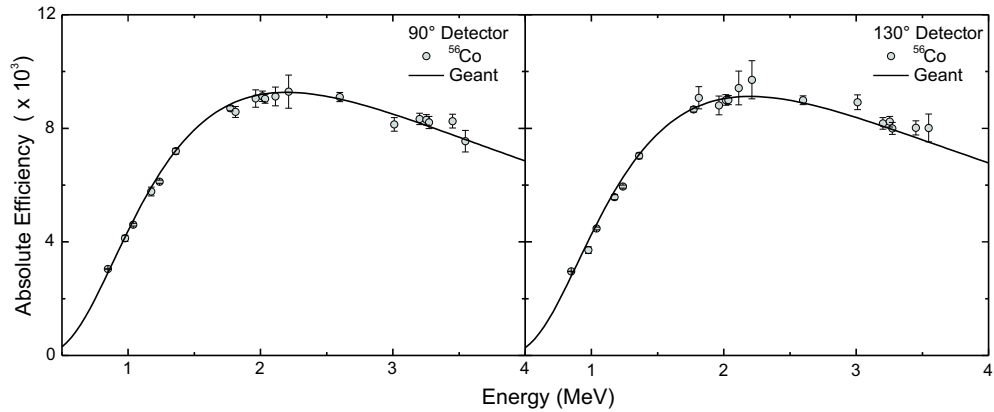
Figure 4.5   Absolute efficiency at $90°$ (left hand side) and at $130°$ (right hand side) for the setup used for the measurement of ^{112}Sn

4.1.3   Spin Determination

Since the aim of this work is to extract the dipole strength distribution, one needs to distinguish the multipolarities of the measured transitions. Using the ratio of the peak in-
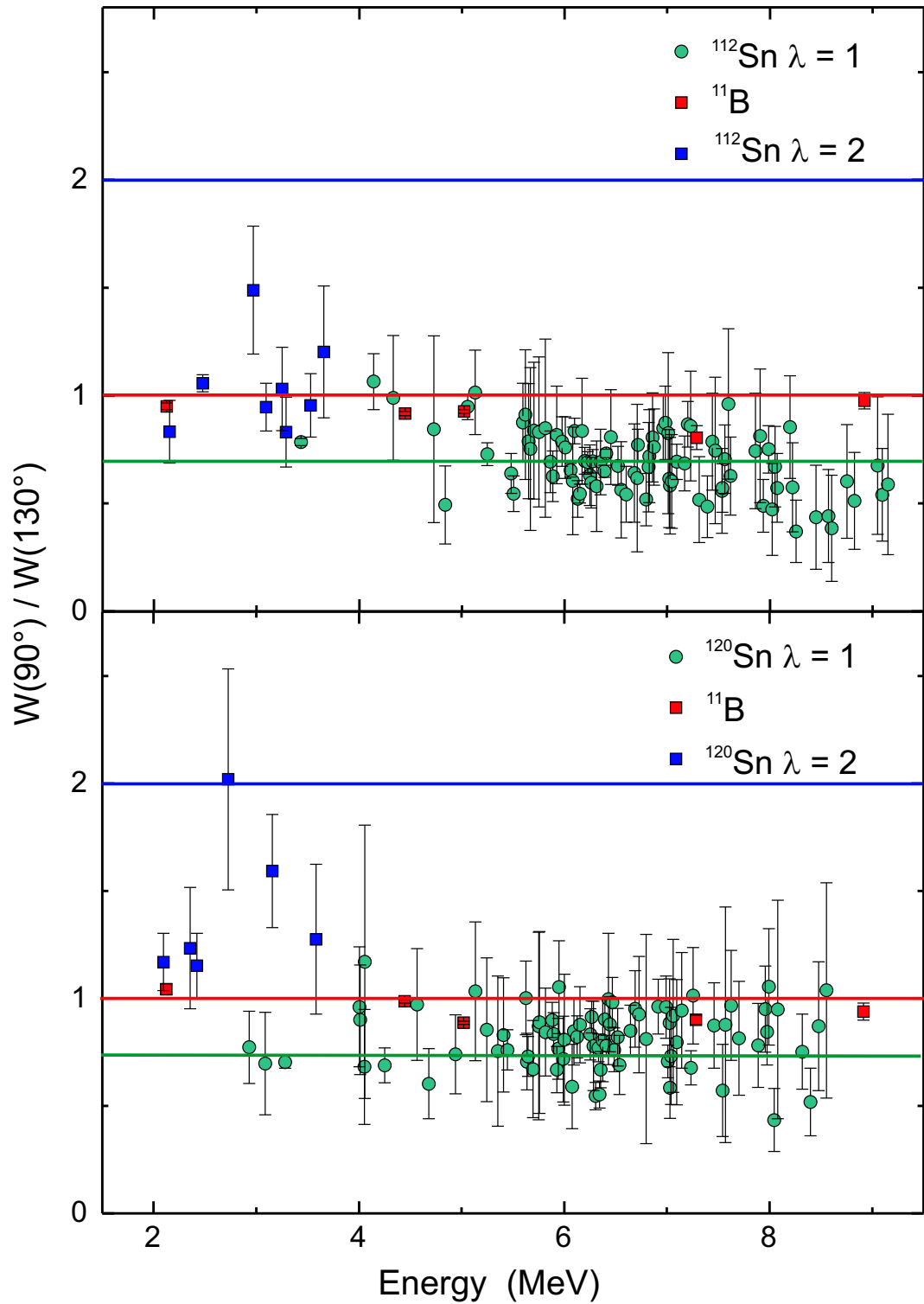
Figure 4.6   Intensity ratio $W(90°)/(130°)$ together with predictions for transition multipolarities $\lambda=1$ or 2 in ^{112}Sn (upper part) and ^{120}Sn (lower part)

tensities at different scattering angles one can extract the multipolarities of the observed transitions. Figure 4.6 shows the intensity ratios of the transitions at 90° and 130° for the ^{112}Sn and ^{120}Sn isotopes. In the Fig. 4.6 the blue and green lines are the predicted values for dipole transitions and quadrupole transitions, respectively. The red line at 1 indicates an isotropic distribution. The red squares correspond to ^{11}B transitions. These transitions should be close to the isotropic line because of their half-integer spin. The blue squares correspond to known (NNDC, 2007) quadrupole transitions. Because of strong interaction in (γ, γ') reaction, some 2^+ states are also observed in the low energy parts of the spectra. These transitions are closer to the isotropic line than expected for a quadrupole transition because of the feeding effect from higher-energy levels discussed below. The green points are dipole transitions for ^{112}Sn (upper part of the figure) and ^{120}Sn (lower part of the figure). Most of the dipole transitions are observed the first time. One can see that all observed ground state transitions above 5 MeV have dipole character.

4.1.4   Photon Flux and Integrated Cross Section

For a calculation of the B(E1) transition strength, one needs to know the photon flux and the integrated cross section. The relation between photon flux and integrated cross section is given by

$$N_\gamma(E_x, E_o) \cdot \varepsilon_{abs}(E_x) = \frac{A_i}{N_{Target} \cdot I_s^i \cdot W_{eff}^i(\theta)} \qquad (4.2)$$

where $N_\gamma(E_x, E_o)$ is the number of photons at an energy E_x for a bremsstrahlungs spectrum with endpoint energy E_0, ε_{abs} is the absolute efficiency at a given excitation energy, A_i is the peak area of the i-th line in NRF spectrum and $W_{eff}^i(\theta)$ is the effective angular correlation function. The product of the bremsstrahlung spectrum and the detector efficiency was simulated using the program GEANT4 (Hasper, private com.) for the endpoint energies of spectra. Since the GEANT4 simulations provide only the energy dependencie of the flux but no absolute values, one has to normalize these to the experimental values of ^{11}B transitions using Eq. (4.2). In the calculation the branching ratios of boron lines are taken to be account. The corresponding excitation energies, spin values of the excited levels and integrated cross sections are given in Table 4.1 and the branching ratios of the

Table 4.1   The transitions of ^{11}B, their spin values and integrated cross sections (NNDC, 2007)

E_x keV	J^π	I_S^0 (10^3eVfm^2)
2124.69	$\frac{1}{2}^-$	5.1(4)
4444.89	$\frac{5}{2}^-$	16.3(6)
5020.31	$\frac{3}{2}^-$	21.9(8)
7285.51	$\frac{5}{2}^+$	9.4(7)
8920.20	$\frac{5}{2}^-$	28.6(14)

^{11}B transitions are shown in Fig. 4.7.

Figure 4.8 shows the fit functions to the simulations of $N_\gamma \cdot \varepsilon_{abs}$ normalized with respect to the ^{11}B lines for ^{112}Sn (upper part) and ^{120}Sn (lower part). The upturned grey triangles and the black triangles are the measured yields of $N_\gamma \cdot \varepsilon_{abs}$ for the ^{11}B lines at 90° and 130°, respectively. The grey lines show the fit functions of GEANT4 simulations for the detector at 90° and the black lines this for the detector at 130°. Once the photon flux is
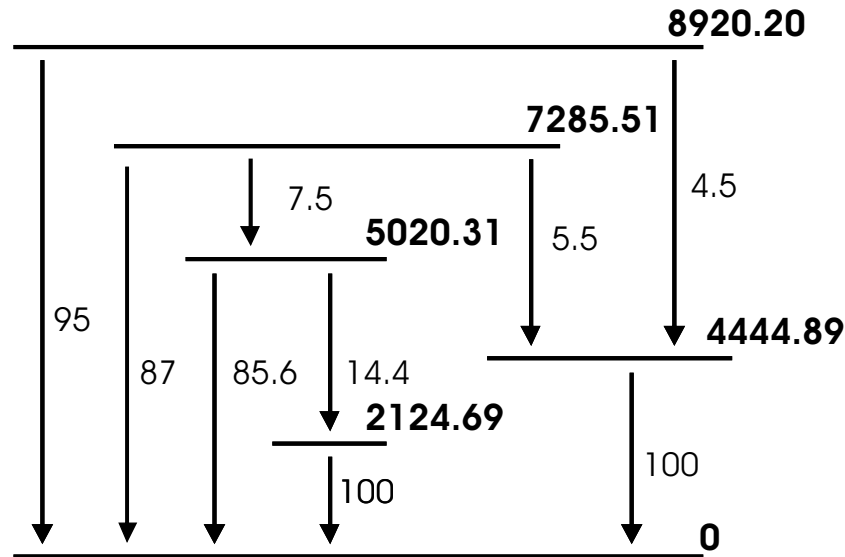
Figure 4.7   Energies of ^{11}B transitions with branching ratios (NNDC, 2007)

known, one can calculate the integrated cross section for every transition. As mentioned before the integrated cross section is proportional to the branching ratio Γ_0/Γ, see Eq. (3.18). Here it is assumed that all measured transitions exclusively decay to the ground state, i.e, the quantity of Γ_0/Γ will be equal to 1. Usually this can be experimentally checked for the branchings to the first excited 2^+ state, but not for higher-lying states.
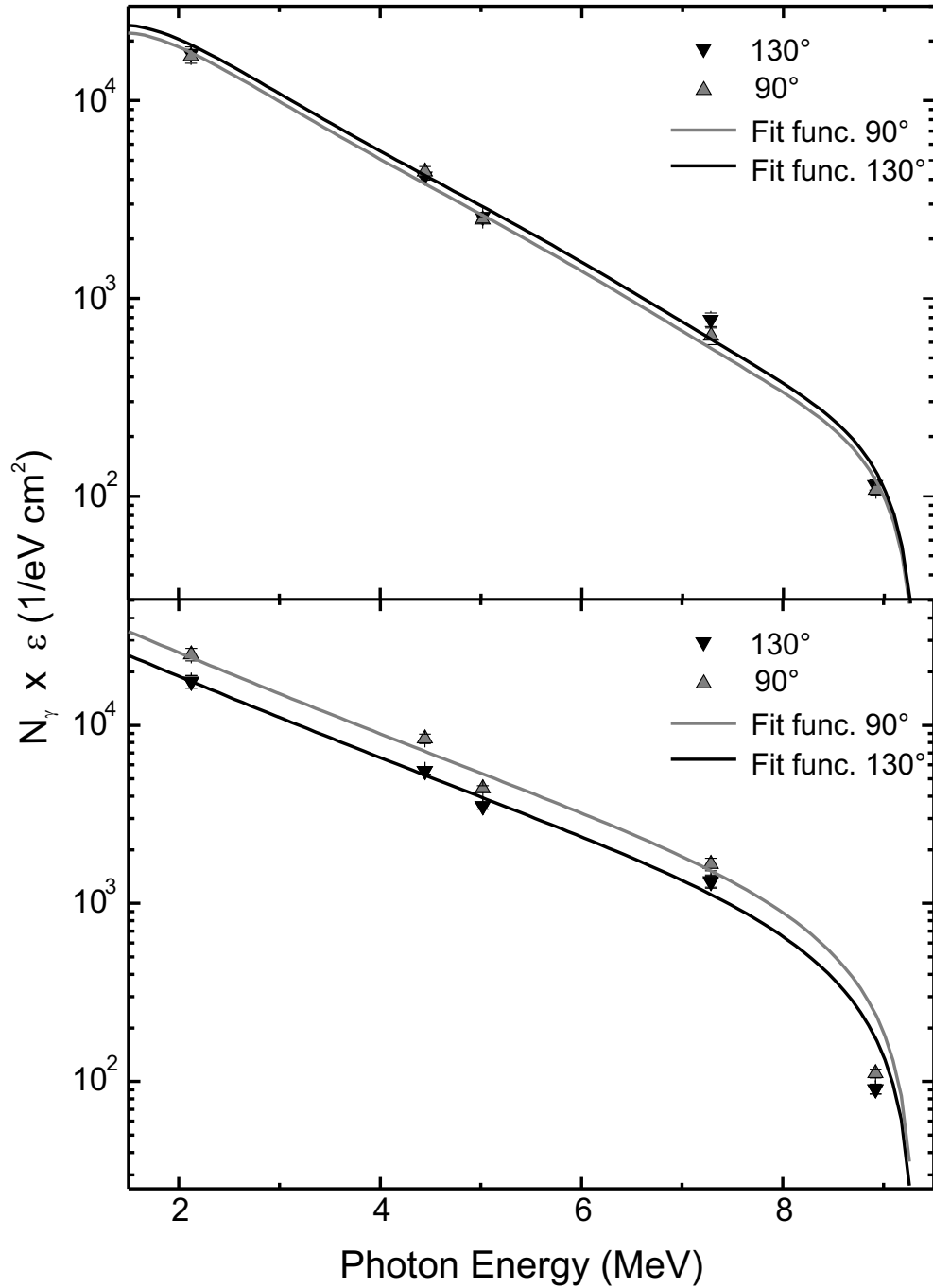
Figure 4.8   Fit functions to the GEANT4 simulations for $N_\gamma \cdot \varepsilon_{abs}$ normalized with respect to the ^{11}B lines for ^{112}Sn (upper part) and ^{120}Sn (lower part)

Furthermore a second assumption is that all excited states have $J^{\pi}=1^{-}$. This is justified because M1 transitions in spherical nuclei are of spin-flip nature and appear at higher energies only (A. Richter, 1991). There is also an experimental test for the PDR in ^{140}Ce where all the parities have been measured (N. Pietralla et al, 2002) and shown to be negative. Using the Eqs. (3.20)-(3.22), the B(E1), B(M1) and B(E2) transition probabilities can be calculated.

4.1.5   Estimation of the Feeding Effect

The possibility of an indirect population of levels by feeding via inelastic transitions from higher-lying states should be taken into account in the calculation of transition strengths. A level can be populated directly by photoabsorption from the ground state and also indirectly by decay from higher-lying states. This can cause an overestimation on the real strength. As already mentioned in case of quadrupole transitions, strong feeding can affect the spin assignment of transitions since the angular distributions of the scattered photons become more isotropic. In this case one has to estimate the feeding effect on the transition strengths. A possible way to investigate the amount of the feeding is to compare the measured transition strengths at different endpoint energies.

The ratio of the measured transition strengths at 9.5 and 7 MeV endpoint energies for ^{112}Sn is displayed in Fig. 4.9. Values larger than 1 indicate a feeding of the transitions. This is the case for a number of transitions especially around 3 and 6.5 MeV. Therefore, the transition strengths are corrected in the results of 9.5 MeV spectrum up to an energy of 6.5 MeV. For ratios exceeding 1, the final values are taken from the measurement at the lower endpoint energy. A spectrum for ^{112}Sn with 5.0 MeV endpoint energy is also available. The comparison between the results of 7 MeV and 5 MeV was made in the diploma thesis of Iryna Poltoratska (Poltoratska, 2005) and it was reported that there is no feeding effect on 7 MeV spectrum.

The same calculations have also been performed for ^{120}Sn isotope. Fig. 4.10 shows the ratio of the measured transition strengths at 9.1 and 7.5 MeV endpoint energies. As seen from the figure obviously the case is different to the previous isotope. The feeding is not observed on the measurement of ^{120}Sn up to 9.1 MeV. The differences between the transition strengths for measurements up to 9.1 and 7.5 MeV are inside of error bars.
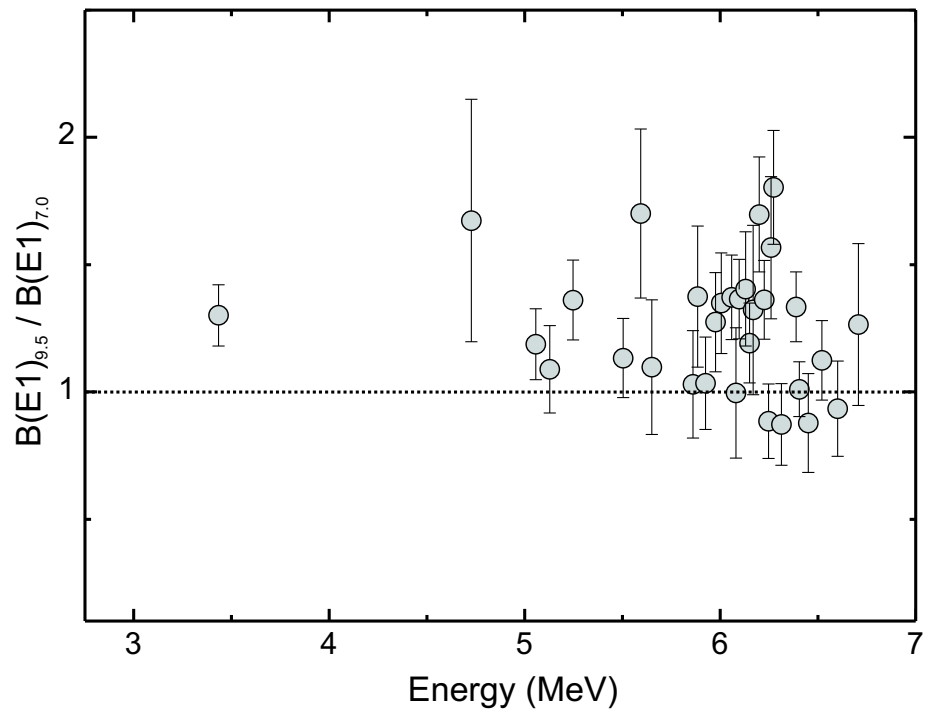
Figure 4.9   Ratio of the B(E1) transition strengths of endpoint energies of 9.5 and 7 MeV for ^{112}Sn
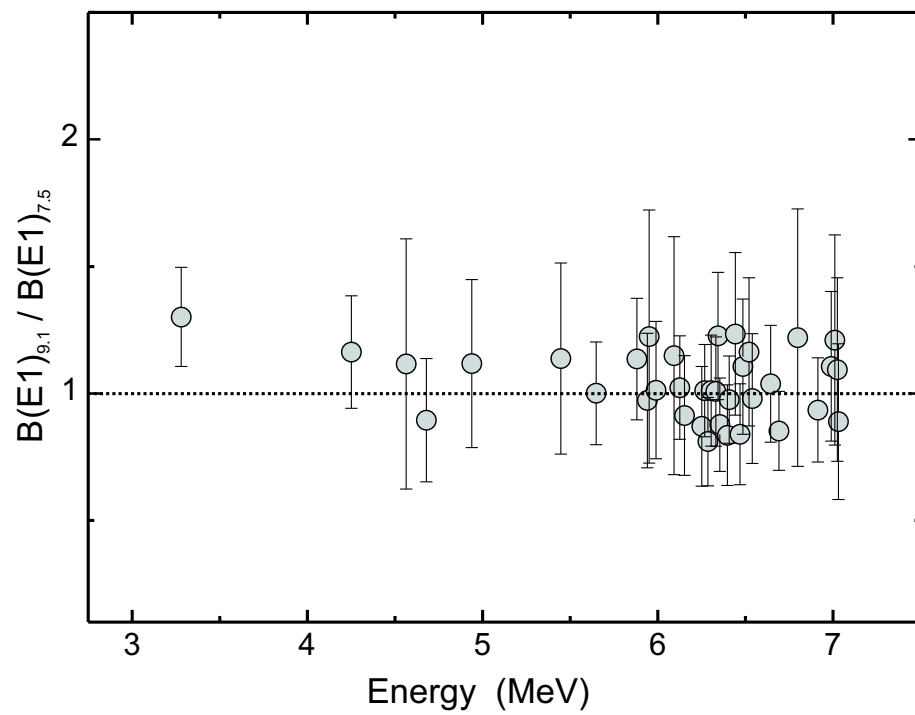
Figure 4.10   Ratio of the B(E1) transition strengths of endpoint energies of 9.1 and 7.5 MeV for ^{120}Sn

Therefore no correction was necessary for the final results of ^{120}Sn and the final results are averaged over both measurements where possible.

4.1.6   Reduced Transition Strengths

The extracted B(E1) transition strengths for ^{112}Sn and ^{120}Sn are shown in Tables 4.2 and 4.3, respectively. The excitation energy E_x and the assigned spin J, the branching ratio Γ_0 and the corresponding reduced transition probabilities of each dipole transition are given. Using the relation between Eq. (3.18) and Eq. (4.2) the elastic transition width Γ_0 of excited levels in the Sn isotopes can be calculated from the measured peak area, the angular correlation, the number of Sn nuclei and the photon flux. Thus, since the energy resolution is very good in these experiments, the main source of systematics errors come from the uncertainties of peak areas. In Table 4.2 and 4.3 the errors are calculated systematically only. One can also add 10 % of error which comes from the normalization of the photon flux.

In total 91 dipole transitions are observed for ^{112}Sn up to 9.5 MeV endpoint energy with as summed of B(E1) transition strength of 0.187(25) e^2fm^2 corresponding to 0.25 % of the EWSR. The number of observed transitions is 72 and the summed B(E1) transition strength is 0.163(31) e^2fm^2 for ^{120}Sn up to 9.1 MeV endpoint energy. The centroid energies of the observed low-lying transitions up to the neutron separation energies are 6.74 MeV and 6.60 MeV for ^{112}Sn and ^{120}Sn, respectively. The two-phonon states are observed in ^{112}Sn at 3434 keV and in ^{120}Sn at 3279 keV which have been already discussed in (Pysmenetska et al., 2005; Bryssinck et al., 1999).

Table 4.2: Transitions observed in ^{112}Sn

E_x (keV)	J^π	Γ_0 (meV)	B(E1)↑ ($10^{-3}e^2fm^2$)
3433.9	1^-	162(15)	11.5(8)
4141.3	1	17(4)	0.7(1)
4162.3	1	44(4)	1.8(2)
4330.4	1	15(3)	0.5(1)
4726.5	1	12(3)	0.3(1)

Continued on next page

Table 4.2 – continued from previous page

E_x (keV)	J^π	Γ_0 (meV)	B(E1)↑ ($10^{-3} e^2 fm^2$)
4837.4	1	28(5)	0.7(1)
5057.1	1	134(13)	3.0(3)
5128.2	1	198(20)	4.2(1)
5246.2	1	166(14)	3.3(3)
5480.5	1	66(11)	1.2(2)
5502.6	1	86(10)	1.5(2)
5593.7	1	43(7)	0.7(1)
5617.6	1	39(7)	0.6(1)
5649.1	1	43(7)	0.7(2)
5666.4	1	23(6)	0.4(1)
5699.9	1	33(7)	0.5(1)
5748.6	1	66(7)	1.0(2)
5812.7	1	34(8)	0.5(1)
5860.7	1	159(27)	2.3(4)
5884.0	1	100(16)	1.4(2)
5924.1	1	112(12)	1.5(2)
5976.6	1	128(14)	1.7(2)
6005.0	1	244(21)	3.2(3)
6059.8	1	470(44)	6.1(6)
6080.9	1	73(15)	0.9(2)
6096.9	1	385(23)	3.6(3)
6129.0	1	115(13)	1.4(2)
6150.4	1	273(28)	3.4(4)
6168.3	1	98(17)	1.2(2)
6198.7	1	179(18)	2.2(2)
6224.3	1	315(26)	3.7(3)
6246.4	1	152(20)	1.8(2)
6259.1	1	130(17)	1.5(2)
6272.6	1	220(21)	2.5(3)

Table 4.2 – continued from previous page

E_x (keV)	J^π	Γ_0 (meV)	B(E1)↑ ($10^{-3}e^2fm^2$)
6313.3	1	251(23)	2.9(4)
6348.7	1	134(17)	1.5(2)
6388.1	1	663(47)	7.3(6)
6404.1	1	1686(120)	18.4(13)
6428.6	1	114(18)	1.2(2)
6450.0	1	109(15)	1.2(2)
6520.7	1	309(33)	3.2(4)
6550.1	1	54(11)	0.6(1)
6601.0	1	173(23)	1.7(2)
6679.9	1	74(14)	0.7(1)
6706.7	1	187(24)	1.8(2)
6715.0	1	156(67)	1.5(3)
6731.9	1	289(51)	2.7(6)
6795.5	1	185(25)	1.7(2)
6818.7	1	139(23)	1.3(2)
6824.2	1	194(32)	1.7(3)
6855.9	1	170(25)	1.5(2)
6871.2	1	189(19)	1.7(2)
6941.2	1	367(41)	3.1(4)
6961.5	1	362(53)	3.1(5)
6982.7	1	246(30)	2.1(3)
7009.8	1	62(15)	0.5(1)
7018.7	1	82(16)	0.7(1)
7025.8	1	86(17)	0.7(1)
7043.1	1	245(42)	2.0(4)
7092.8	1	524(48)	4.2(4)
7167.2	1	363(42)	2.8(3)
7198.2	1	578(75)	4.4(6)
7228.1	1	164(27)	1.2(2)

Table 4.2 – continued from previous page

E_x (keV)	J^π	Γ_0 (meV)	B(E1)↑ ($10^{-3}e^2fm^2$)
7311.1	1	138(28)	1.0(2)
7389.9	1	183(30)	1.3(2)
7438.6	1	275(42)	1.9(3)
7444.1	1	233(37)	1.6(3)
7468.3	1	186(45)	1.3(3)
7531.3	1	429(62)	2.9(4)
7537.2	1	770(82)	5.2(6)
7559.1	1	323(43)	2.1(3)
7594.5	1	205(31)	1.3(2)
7615.3	1	257(41)	1.7(3)
7859.5	1	207(35)	1.2(2)
7904.7	1	196(40)	1.1(2)
7936.7	1	272(39)	1.6(2)
7988.2	1	606(62)	3.4(3)
8020.7	1	412(67)	2.3(4)
8051.6	1	396(60)	2.2(3)
8069.6	1	482(65)	2.6(4)
8194.5	1	518(75)	2.7(6)
8218.2	1	262(48)	1.4(2)
8253.6	1	177(38)	0.9(2)
8448.6	1	147(41)	0.7(2)
8568.9	1	166(43)	0.8(2)
8600.4	1	118(35)	0.5(2)
8750.2	1	249(56)	1.1(2)
8823.4	1	278(64)	1.2(3)
9050.5	1	413(108)	1.6(4)
9095.3	1	268(65)	1.0(2)
9150.1	1	240(75)	0.9(3)
9329.8	1	599(138)	2.1(5)

Table 4.3: Transitions observed in ^{120}Sn

E_x (keV)	J^π	Γ_o (meV)	B(E1)↑ $(10^{-3}e^2fm^2)$
3279.4	1^-	137(14)	8.6(9)
4251.0	1	73(10)	2.7(4)
4564.8	1	36(8)	1.0(2)
4679.7	1	52(10)	1.5(3)
4939.0	1	36(8)	0.9(2)
5245.4	1	22(7)	0.4(1)
5354.4	1	37(13)	0.7(2)
5408.2	1	54(13)	1.0(2)
5447.2	1	126(21)	2.2(4)
5638.0	1	109(18)	1.8(3)
5647.8	1	172(23)	2.7(4)
5685.2	1	78(20)	1.2(3)
5697.3	1	67(17)	1.0(3)
5753.0	1	35(13)	0.5(2)
5758.0	1	42(15)	0.6(2)
5818.0	1	127(25)	1.8(4)
5882.1	1	280(40)	3.9(6)
5895.4	1	198(26)	2.8(4)
5927.7	1	165(25)	2.3(3)
5940.7	1	230(44)	3.1(6)
5950.2	1	139(35)	1.9(5)
5989.8	1	203(38)	2.7(6)
6001.7	1	168(48)	2.2(6)
6076.2	1	82(21)	1.1(3)
6093.5	1	110(24)	1.4(3)
6127.1	1	248(35)	3.1(4)
6152.5	1	127(23)	1.6(3)
6252.4	1	255(48)	3.0(6)

Table 4.3 – continued from previous page

E_x (keV)	J^π	Γ_0 (meV)	B(E1)↑ ($10^{-3}e^2fm^2$)
6267.0	1	350(44)	4.1(5)
6285.8	1	160(31)	1.8(4)
6305.9	1	270(37)	3.1(4)
6332.6	1	363(54)	4.1(6)
6344.9	1	370(50)	4.2(6)
6353.7	1	259(38)	2.9(4)
6375.0	1	118(23)	1.3(3)
6397.0	1	240(40)	2.6(4)
6408.3	1	456(55)	5.0(6)
6432.3	1	142(28)	1.5(3)
6443.7	1	299(52)	3.2(6)
6469.7	1	375(62)	4.0(7)
6485.8	1	409(67)	4.3(7)
6520.7	1	186(32)	1.9(3)
6539.5	1	219(40)	2.2(4)
6644.3	1	438(68)	4.3(7)
6691.0	1	206(41)	2.0(4)
6727.3	1	238(55)	2.2(5)
6898.9	1	508(163)	4.6(15)
6914.8	1	374(58)	3.2(5)
6990.4	1	376(68)	3.2(6)
7009.9	1	480(98)	4.0(8)
7025.0	1	216(41)	1.8(3)
7031.5	1	176(35)	1.5(3)
7038.9	1	160(38)	1.3(3)
7061.9	1	164(48)	1.3(4)
7095.6	1	242(65)	1.9(5)
7144.5	1	259(58)	2.0(5)
7235.1	1	495(64)	3.7(5)

Table 4.3 – continued from previous page

E_x (keV)	J^π	Γ_0 (meV)	B(E1)↑ ($10^{-3}e^2fm^2$)
7255.1	1	465(88)	3.5(7)
7460.1	1	175(33)	1.2(2)
7543.1	1	172(49)	1.1(3)
7569.2	1	309(140)	2.0(9)
7624.9	1	190(40)	1.2(3)
7701.2	1	229(57)	1.4(4)
7889.0	1	312(62)	1.8(4)
7958.6	1	523(93)	3.0(5)
7975.6	1	606(98)	3.4(6)
7994.5	1	237(48)	1.3(3)
8044.3	1	120(30)	0.7(2)
8079.7	1	258(100)	1.4(5)
8318.3	1	498(96)	2.5(5)
8399.5	1	450(100)	2.2(5)
8478.3	1	304(80)	1.4(4)
8554.9	1	447(139)	2.0(6)

4.1.7   Systematics of the E1 Strength in Stable Tin Isotopes

Systematics studies of electric dipole (E1) response are very important to understand a possible collective character of the low-energy E1 strength. Thus, the present results are compared with previous measurements in the even-even tin isotopes [116,124]Sn (Govaert et al., 1998) obtained with the NRF method up to 10 MeV endpoint energy. Figure 4.11 shows the distribution of the B(E1) strengths in [112,116,120,124]Sn. A resonance-like structure shape is observable in the distributions of the transition strengths for every isotope and the maximum transition strengths are located approximately in the same energy region. Major differences appear above 7 MeV, eventually because of different neutron separation energies of the isotopes. The summed B(E1) transition strengths and centroid
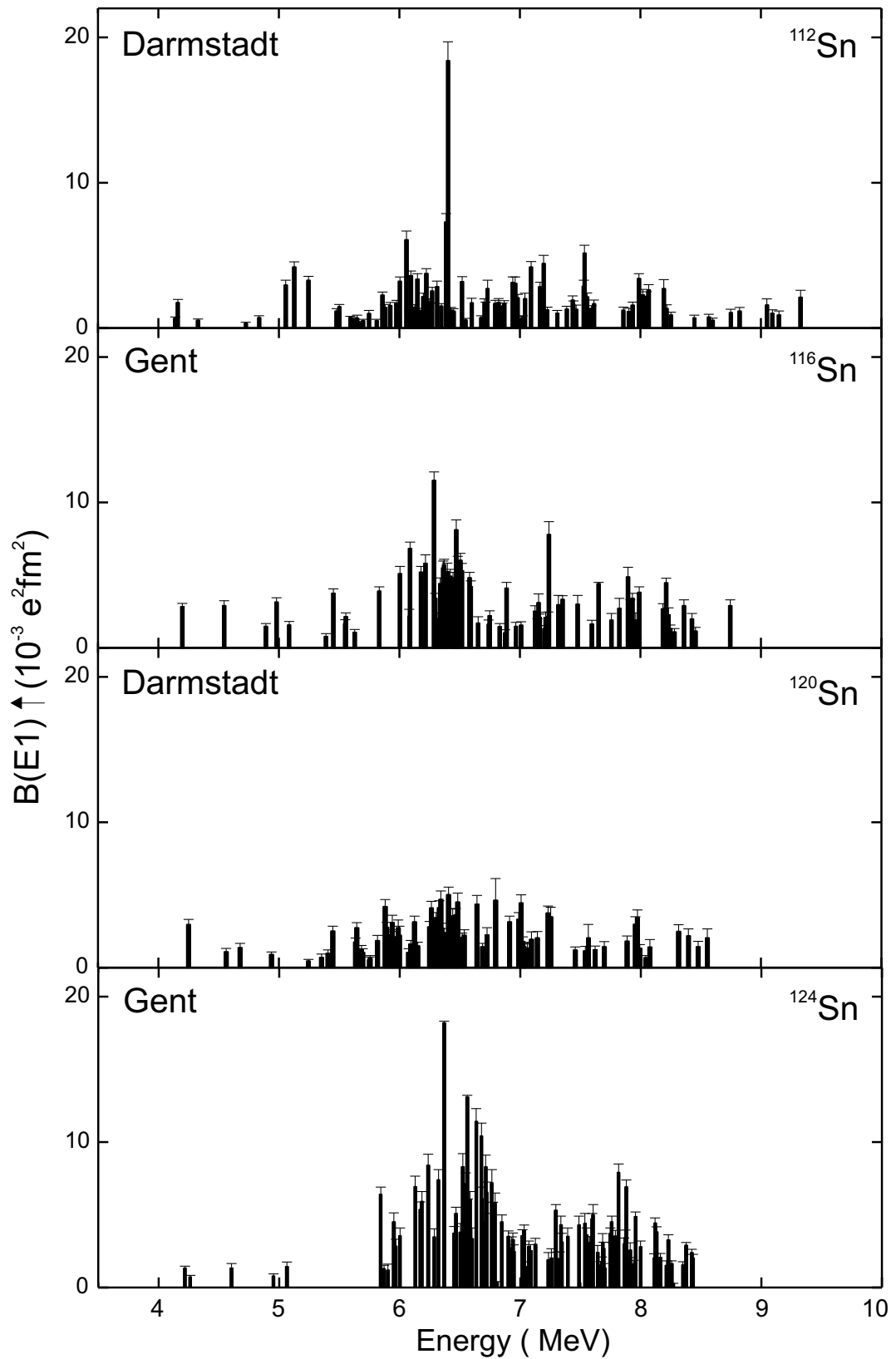
Figure 4.11   Comparison of the B(E1) strength in ^{112,116,120,124}Sn

energies are summarized for the stable ^{112,116,120,124}Sn isotopes in Table 4.4.

Table 4.4   The sum of B(E1) transition strengths for ^{112,116,120,124}Sn

Isotope	$\sum$B(E1) e^2fm^2	E_C (MeV)	E_0 (MeV)
^{112}Sn	0.187(25)	6.7	9.5
^{116}Sn	0.233(28)	6.7	10.0
^{120}Sn	0.163(31)	6.6	9.1
^{124}Sn	0.379(45)	7.0	10.0

4.2   Fluctuation Analysis

According to theoretical predictions discussed in the next section, the summed B(E1) strengths should increase with the number of neutrons. But the experimental results show that ^{120}Sn has the lowest summed strength and transitions are more fragmented compared to other even stable tin isotopes. The fragmentation is visible even from the spectra of ^{120}Sn. This made us to think about unresolved strength which could be hidden in the background. The extraction of this type of strength is not possible with usual analysis method. To determine unresolved strength, a fluctuation analysis was applied for first time on (γ, γ') spectra to investigate B(M1) scissors mode strength in odd-mass nuclei (Enders et al., 1997; Huxel et al, 1999). In the following section the fluctuation analysis is explained and applied to the (γ, γ') spectra of ^{112,120}Sn.

4.2.1   Theoretical Models

An essential ingredient to the fluctuation analysis is the level density which has to be taken from models. In the present work, two different types are considered, namely an empirical and a microscopic approach.

4.2.1.1   Back-Shifted Fermi Gas Model

Nuclear Level Densities (NLD) are important quantities in nuclear physics. For example predicting the distribution of all the excited levels in nuclei helps to understand this complicated quantum system. Besides, the NLD represent very important ingredients in statistical model calculation of nuclear reactions cross sections which are needed for many application in astrophysics and also fission or fusion reactor designs.In the present work NLD are needed to determine the nonresonant background in (γ, γ') spectra.

Most of the calculations of NLD are modifications and extensions of the Fermi gas model including pairing and shell effects in a semi-empirical way (Gilbert, 1965), the so-called back-shifted Fermi gas model (BSFG). The NLD dependence on energy E_x and spin J is given in a separable form

$$\rho(E_x, J, \pi) = \frac{1}{2}\rho(E_x)f(J) \tag{4.3}$$

$$f(J) = exp[-\frac{J^2}{2\sigma^2}] - exp[-\frac{(J+1)^2}{2\sigma^2}]. \tag{4.4}$$

The factor 1/2 in Eq. (4.3) results from the assumption of parity independence.

In the BSFG model (Gilbert, 1965) the energy part is given by

$$\rho(E_x) = \frac{\exp[2\sqrt{a(E_x - E_1)}]}{12\sqrt{2}\sigma a^{1/4}(E_x - E_1)^{5/4}}. \tag{4.5}$$

Here σ is the spin cut-off parameter which depends on the rigid-body moment of inertia of the nucleus. The formula is given by (Zhongfu, 1991)

$$\sigma^2 = 0.0146A^{5/3}\frac{1 + \sqrt{1 + 4a(E_x - E_1)}}{2a} \tag{4.6}$$

where E_1 is the energy backshift and a is the NLD parameter in MeV^{-1}. The quantity a represents the shell effect taken to be independent of the energy. It means that the shell effect plays a role at higher energies in the same way as at low energies. However,

microscopic calculations of the NLD show that the shell effects are stronger at low energies. Thus, an energy dependent description was needed to define for a parameter which includes the quenching of the shell effect (Ignatyuk et al.,1975; 1979),

$$a(E_x, Z, N) = \tilde{a}[1 + \frac{S(Z,N) - \Delta}{E_x - E_2 f(E_x - E_2)}]. \tag{4.7}$$

Here, $\tilde{a}$ is the asymptotic value of the a parameter

$$\tilde{a} = \alpha A + \beta A^{2/3} \tag{4.8}$$

The function f has been proposed (Ignatyuk et al.,1975; Rauscher et al.,1997) to have the following term

$$f(E_x - E_2) = 1 - exp[-\gamma(E_x - E_2)]. \tag{4.9}$$

In these calculations α, γ, β are the free parameters which can be determined by fitting to experimental data. In Eq.(4.7), $S(Z, N)$ is given as a shell correction and is defined by

$$S(Z,N) = M_{exp} - M_{LD}, \tag{4.10}$$

where M_{exp} is the experimental mass and M_{LD} is the mass calculated with a macroscopic liquid-drop formula.

The following equation gives the total number of levels as a function of excitation energy E_x,

$$N_0(E_x, J) = \int_0^{E_x} \rho(E, J) dE. \tag{4.11}$$

Finally, the mean level spacing $\langle D \rangle = 1/\rho$ in an energy interval $[E_x^a, E_x^b]$ can be expressed as (Kalmykov, 2004)

$$\langle D \langle = \frac{E_x^b - E_x^a}{N_0(E_x^b, J) - N_0(E_x^a, J)}. \tag{4.12}$$

Two different parameterizations of the BSFG model are selected for the present analysis. The first approach called BSFG1 (Rauscher et al., 1997) has much higher predictive power in nuclei near the valley of stability and is used in astrophysical nucleosynthesis calculations. The second approach called BSFG2 (Egidy et al., 2005) is more reliable for an extrapolation towards exotic nuclei since the model parameters are derived only from precise mass data (Audi et al., 2003; Möller et al., 1995).

4.2.1.2 Hartree-Fock-BCS Model

Alternatively, a microscopic statistical model is used to obtain the NLD. This model is based on the ground-state structure properties predicted within the Hartree-Fock-BCS (HF-BCS) approach (Demetriou et al., 2001). The microscopic model includes a consistent treatment of the shell effects, pairing correlations, deformation and collective excitations. The model can predict the experimental neutron resonance spacing with an accuracy comparable to that of the phenomenological BSFG type of models. The microscopic NLD also gives reliable extrapolations to low energies where experimental data on the cumulative number of levels are available.

The spin-independent level density is determined by the partition method

$$\rho(E_x) = \frac{exp[S(E_x)]}{(2\pi)^{3/2}\sqrt{D(E_x)}}. \tag{4.13}$$

The entropy S and excitation energy E_x at a temperature T are derived from the summation on the degenerate single-particle levels ε_q^k (where $q=$ n, p stands for neutrons or protons). For details see (Demetriou et al., 2001). In the case of spherical nuclei, the spin-dependent level density can be given as a function of the total level density $\rho(E_x)$ by

$$\rho(E_x, J) = \frac{2J+1}{2\sqrt{2\pi}\sigma^3} exp[\frac{-J(J+1)}{(2\sigma^2)}]\rho(E_x) \tag{4.14}$$

and spin cut-off parameter for the spherical nuclei is given by

$$\sigma^2(T) = \frac{1}{2} \sum_{q=n,p} \sum_k m_q^{k^2} sech^2(\frac{E_q^k}{2T}) \tag{4.15}$$

which is obtained from the summation on the angular momentum projection m_q^k. Here, E_q^k is the quasiparticle energy which depends on the single particle levels, the BCS gap parameter and the chemical potential as a function of the pairing strength. The HF calculations are fit to the full set of measured masses (Tondeur et al., 2000; Goriely et al., 2001) for the determination of the nucleon interaction. This should make the corresponding HF predictions particularly reliable (Demetriou et al., 2001).

4.2.2 Fluctuation Analysis Method

The fluctuation analysis method was originally established for β-delayed particle emission spectra (Hansen, 1979), subsequently used for the giant resonant spectra from electron scattering (Müller et al., 1982; Kilgus et al., 1987) and also applied successfully to γ-ray spectra to search for unresolved M1 strength in deformed odd-mass nuclei (Enders et al., 1997; Huxel et al., 1999).

The method is applicable in the region where the mean level spacing $\langle D \rangle$ is smaller than the experimental energy resolution ΔE and at the same time the mean level width $\langle \Gamma \rangle$ is smaller than $\langle D \rangle$ and ΔE, i.e.

$$\langle \Gamma \rangle \leq \langle D \rangle < \Delta E \tag{4.16}$$

The case of $\langle \Gamma \rangle > \langle D \rangle$ is called Ericson fluctuations (Ericson, 1960) which stem from the coherent overlap of excitations whose line widths $\langle \Gamma \rangle$ exceed the average level spacing.

Two assumptions are used for the calculation of experimental level densities. Because of strong configuration mixing of levels with same spin and parity in a highly excited nucleus, the probability for a certain spacing between neighboring states is assumed to follow the Wigner distribution (Wigner, 1965)

$$P_w(s) = \frac{\pi s}{2} \exp(-\frac{\pi s^2}{4}), \tag{4.17}$$

where

$$s = \frac{D}{\langle D \rangle}. \tag{4.18}$$

This distribution has a maximum around the mean value and shows so-called level repulsion, *i.e.* a suppression of small distances between close neighboring levels. The transition strengths obey a Porter-Thomas distribution (Porter et al., 1956)

$$P_{PT}(r) = \frac{1}{\sqrt{2\pi r}} exp(\frac{-r}{2}), \tag{4.19}$$

$$r = \frac{\Gamma_0}{\langle \Gamma_0 \rangle}. \tag{4.20}$$

This equation predicts that weak transitions are more likely.

For the application of the fluctuation analysis technique one has to assure that the spectrum contains only the information directly related to the ground state transition widths Γ_0 (Enders et al., 1998). One can extract the unresolved strength from the fluctuations of this measured spectrum with the following steps shown in Fig. 4.12. In the uppermost part (a) the spectrum is shown with an energy resolution maximum $\Delta(E) \approx 10$ keV and the selected background. Firstly the background subtracted spectrum is smoothed by convolution with a Gaussian function $\sigma_>$ to remove gross structure in the spectrum. This value should be selected bigger than the experimental energy resolution. This new spectrum is called as $g_>(x)$ and shown with by red line in Fig. 4.12 (b). In order to diminish the contribution of counting statistics to the fluctuations, the spectrum is also folded with a Gaussian function with width $\sigma_<$ smaller than experimental energy resolution which produces the $g_<(x)$ spectrum shown in Fig. 4.12 (b) by the black line. The so-called stationary spectrum is defined as the ratio of the $g_<(x)$ and $g_>(x)$ spectra.
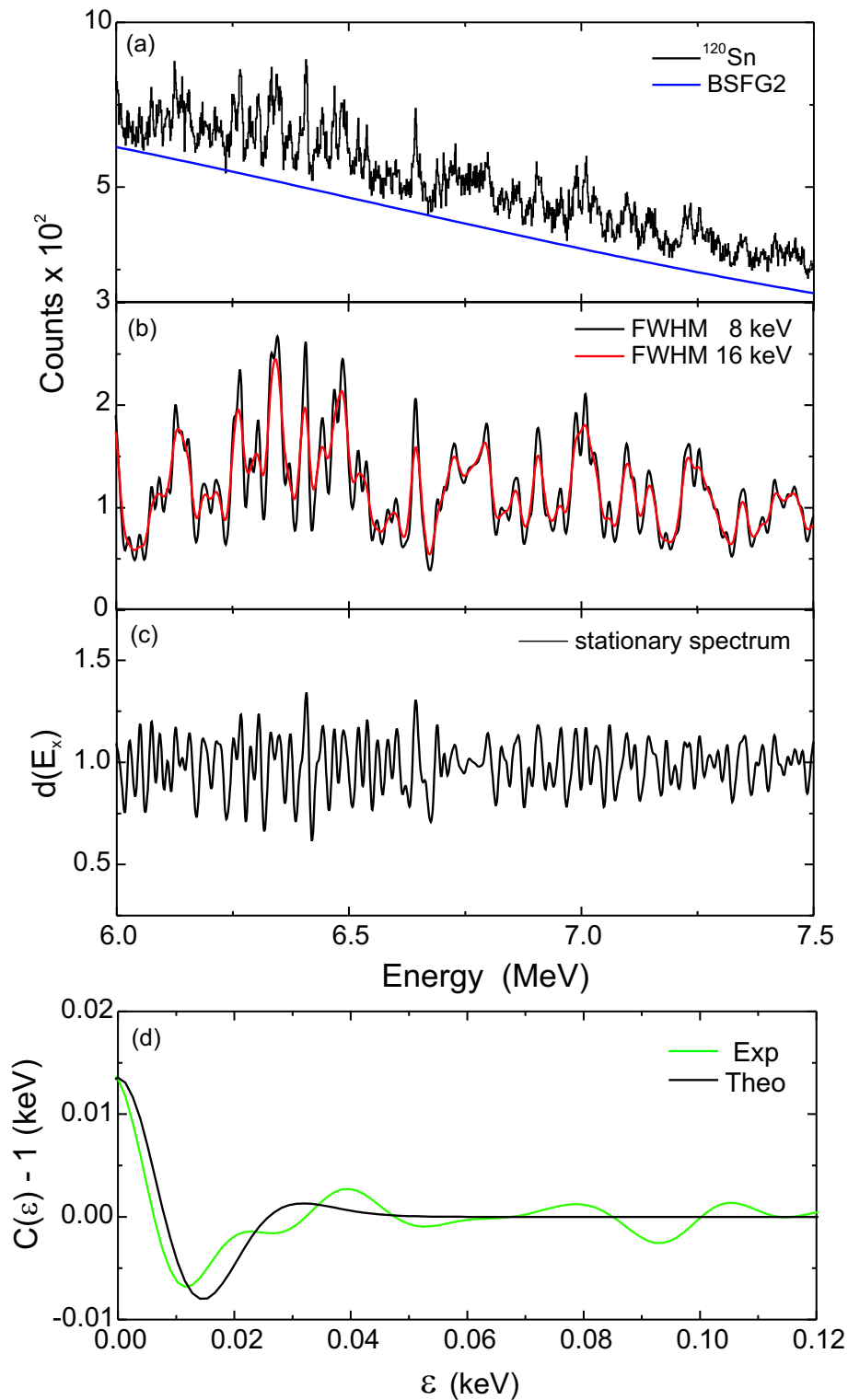
Figure 4.12   (a) Spectrum of the ^{120}Sn(γ, γ') reaction and selected background, (b) smoothed spectra with 16 keV and 50 keV FWHM, (c) stationary spectrum $d(E_x)$ which conforms the local fluctuations only, (d) theoretical and experimental autocorrelation functions

$$d(E_x) = \frac{g_<(x)}{g_>(x)}.$$ (4.21)

The stationary spectrum $d(E_x)$ shows local fluctuations in a given energy interval displayed in Fig. 4.12 (c). A measure of the fluctuations is given by the autocorrelation function of the stationary spectrum

$$C(\varepsilon) = \langle d(E_x)d(E_x+\varepsilon)\rangle$$ (4.22)

where the brackets indicate averaging over the interval for which the analysis is performed, and ε is the shift parameter in the autocorrelation. The experimental autocorrelation function can be well approximated (Jonson et al., 1976; Hansen, 1979) by the analytical expression

$$C(\varepsilon) - 1 = \frac{\alpha \cdot \langle D\rangle}{2\sigma\alpha\sqrt{\pi}} \times f(\varepsilon, \sigma_>, \sigma_<)$$ (4.23)

where $\langle D\rangle$ is the average level spacing and the function f depends on experimental parameters only. The background is now varied until the theoretical and experimental autocorrelations agree at $\varepsilon = 0$, where there is a simple linear relation between $C(0)$ and the product $\alpha\langle D\rangle$ since the function f is normalized $f(\varepsilon = 0)=1$. The experimental and theoretical autocorrelation functions are plotted in Fig. 4.12 (d). The differences between the experimental and theoretical autocorrelation functions for finite ε may be due to errors induced by the finite range of the energy interval. The quantity $\alpha = \alpha_D + \alpha_I$ represents the sum of the variances for the level spacing α_D and the strength distribution α_I, respectively. For a single class of states with given spin and parity, alpha$_D$ and alpha$_I$ are known (Guhr et al., 1998), and $\alpha = 0.273 + 2.0$. If there are levels of n mixed spin and parities the variance from the overlap of the distributions for each J^π has to be defined. The variance α_I is given by (Huxel, 1997)

$$\alpha_I = 3 \cdot \frac{\sum_{i=1}^{n} \frac{(N_i\langle\Gamma_0\rangle_i)^2}{N_i} \cdot \sum_{i=1}^{n} N_i}{\sum_{i=1}^{n} N_i\langle\Gamma_0\rangle_i}$$ (4.24)

where N_i and $\langle\Gamma_0\rangle_i$ the average number of states and ground-state transition widths of type i in the energy interval under consideration.

4.2.3   Application to Photon Scattering Spectra

There are two different approaches in the fluctuation analysis. The first one is a determination of experimental level densities assuming a certain shape of the non-resonant background. It is not always possible to know exactly the background sources and shape. In this case a discrete wavelet analysis provides a method for a model-independent extraction of the background (Kalmykov et al., 2006; 2007). The second approach assumes that the level densities are known for a nucleus with reasonable accuracy which to allow an "inverse" application of the fluctuation analysis. If the level density is assumed to be defined, e.g. calculated by a theoretical model, one can determine the background by varying its shape and magnitude in such a way that the experimental value $C(\varepsilon = 0)$ becomes equal to the theoretical one. However, it should be taken into account that the value of the autocorrelation function is much more sensitive to the area under the background than to its shape.

After the extraction of B(E1) transition strengths from the spectra of ^{112,120}Sn, the question arises if there is unresolved strength hidden in the background due to fragmentation of the transitions. Therefore the fluctuation analysis is applied to the (γ, γ') spectra of ^{112,120}Sn. Firstly the discrete wavelet transform method, which is the model independent way, was tried. However, it was not possible to extract the real background because the method requires a certain signal-to-background ratio which cannot be reached in this type of experiment. However, the level densities can be determined for ^{112,120}Sn by the BSFG1, BSFG2 and HF-BCS theoretical models therefore the second approach an "inverse" application of fluctuation analysis which is explained above is selected to determine the backgrounds of ^{112}Sn and ^{120}Sn spectra at different angles.

For the application of the fluctuation analysis technique one has to assure that the spectrum contains only the information directly related to the ground state transition widths of the nucleus under investigation (Enders et al., 1998). Therefore ^{11}B lines and escape peaks have to be removed from the spectrum. These removed photopeaks are determined by fitting agaussian with linear background, low and high exponential functions (Longo-
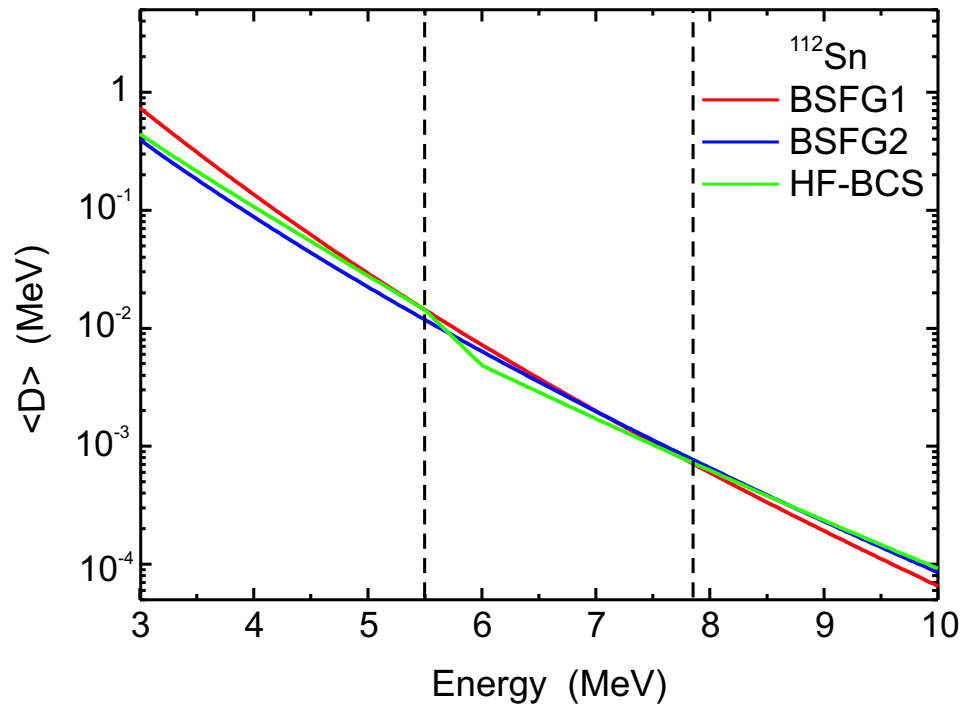
Figure 4.13   Calculated level spacing, $<D>$ for ^{112}Sn from models of BSFG1, BSFG2 and HF-BCS. The dashed lines indicate the interval of application the fluctuation analysis.

Figure 4.14   Calculated level spacing, $<D>$ for ^{120}Sn from models of BSFG1, BSFG2 and HF-BCS. The dashed lines indicate the interval of application the fluctuation analysis.
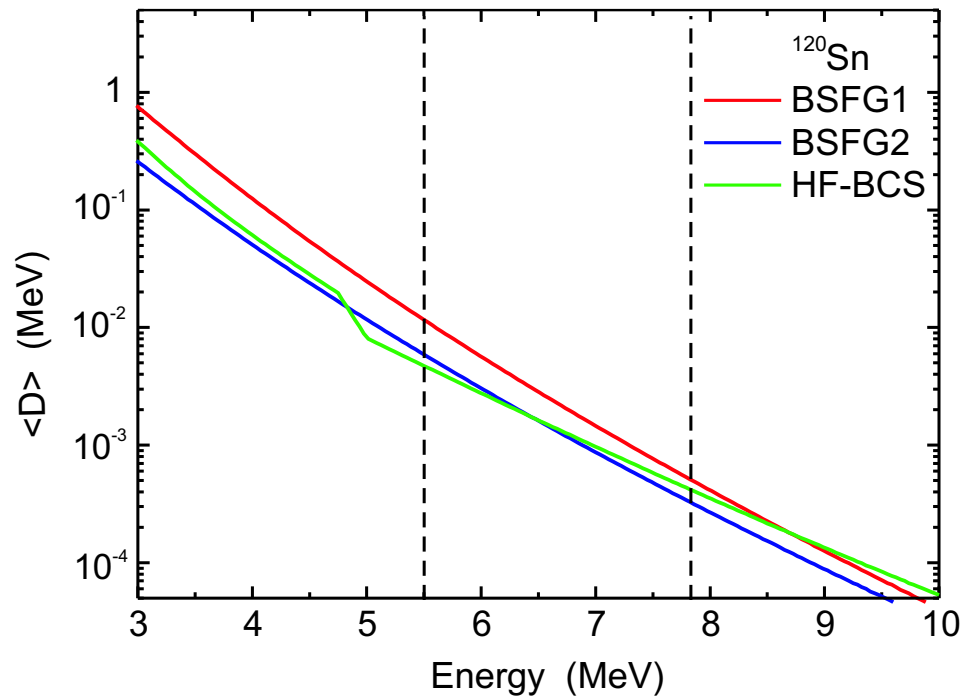
ria, 1990) and are subtracted from spectra.

As pointed out before, the analysis is restricted to the energy region where the mean level spacing is smaller than the experimental energy resolution. This necessary condition is fulfilled for ^{112,120}Sn spectra approximately above 5.5 MeV where also E1 transitions start to increase in numbers. The level spacings are calculated from three different theoretical models BSFG1, BSFG2 and HF-BCS which can be seen in Fig. 4.13 for ^{112}Sn and in Fig. 4.14 for ^{120}Sn.

Considering an inverse application of the fluctuation analysis, the region is divided in 200 keV intervals, where the background is assumed to be constant. These intervals are individually fitted and then a smooth curve is drawn through the points defined by the center of the intervals and the result curves are shown in Figs. 4.15 - 4.18. This process is applied on the spectra at 90° and 130° for both isotope. The analysis is performed in an energy region of 5.5 to 7.8 MeV. At higher energies the extraction of experimental level densities are no longer reliable because of an overlapping in the widths and a lack of statistics. The final backgrounds are plotted for ^{112}Sn in Fig. 4.15, Fig. 4.16 and for ^{120}Sn in Fig. 4.17, Fig. 4.18 at 90° and 130° respectively. In these figures red lines, blue lines and green lines correspond to the determined backgrounds assuming the NLD from the BSFG1, BSFG2 and HF-BCS models, respectively. Although the three backgrounds from the models are calculated independently, they show almost the same results. To determine the strength from the spectrum, the area above the background is integrated as B(E1) transition strength. In order to calculate the total strength for one NLD model, an average is taken over results from 90° and 130°. Extracted strengths from different angles have similar amounts. The consistency of the results at 90° and 130° is also very important proof to show the reliability of this analysis method. In this case three different total strengths from the BSFG1, BSFG2 and HF-BCS have been extracted for one isotope. For the final result an average is taken over these results.

In the integrated region SE peaks should be taken to be account. The contribution of SE peaks is estimated by a GEANT4 simulation (Hasper, private com.) which calculates the escapes from germanium detectors used in the present experiments. The results for the ratio of SE to photopeak with BGO and a fit function are displayed in Fig. 4.19 in

Figure 4.15 ^{112}Sn spectrum at 90° and calculated backgrounds according to the BSFG1, BSFG2 and HF-BCS level density models

Figure 4.16 ^{112}Sn spectrum at 130° and calculated backgrounds according to the BSFG1, BSFG2 and HF-BCS level density models
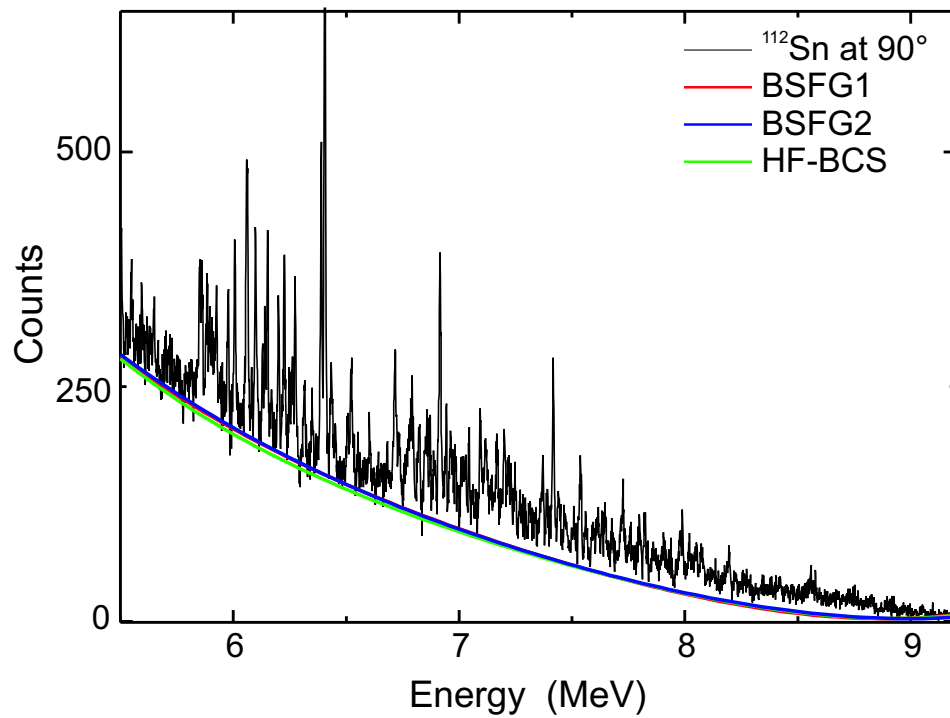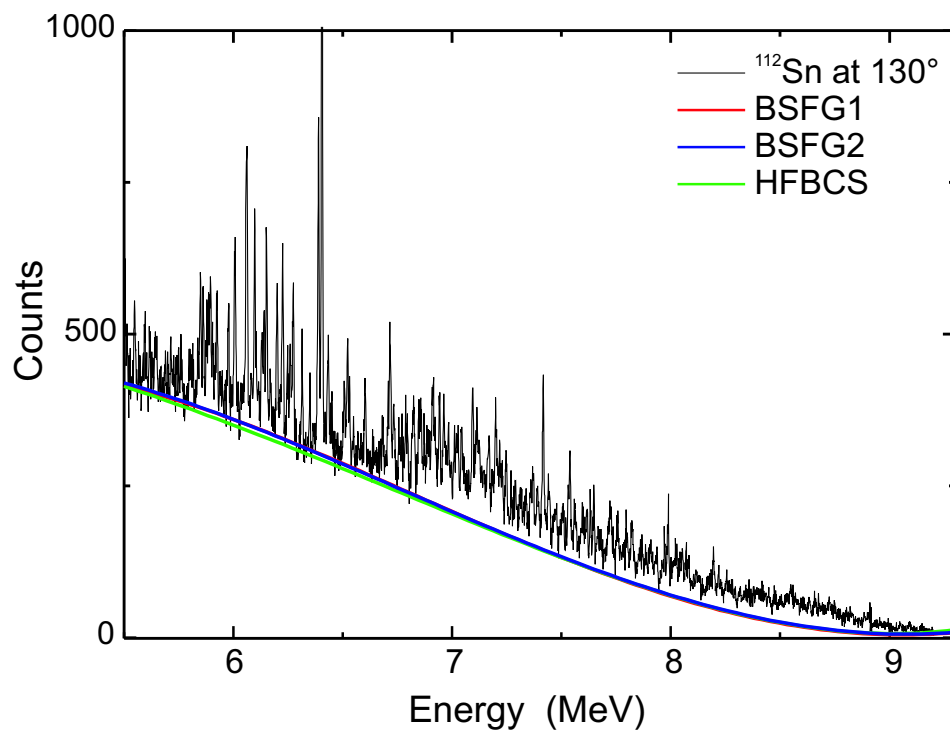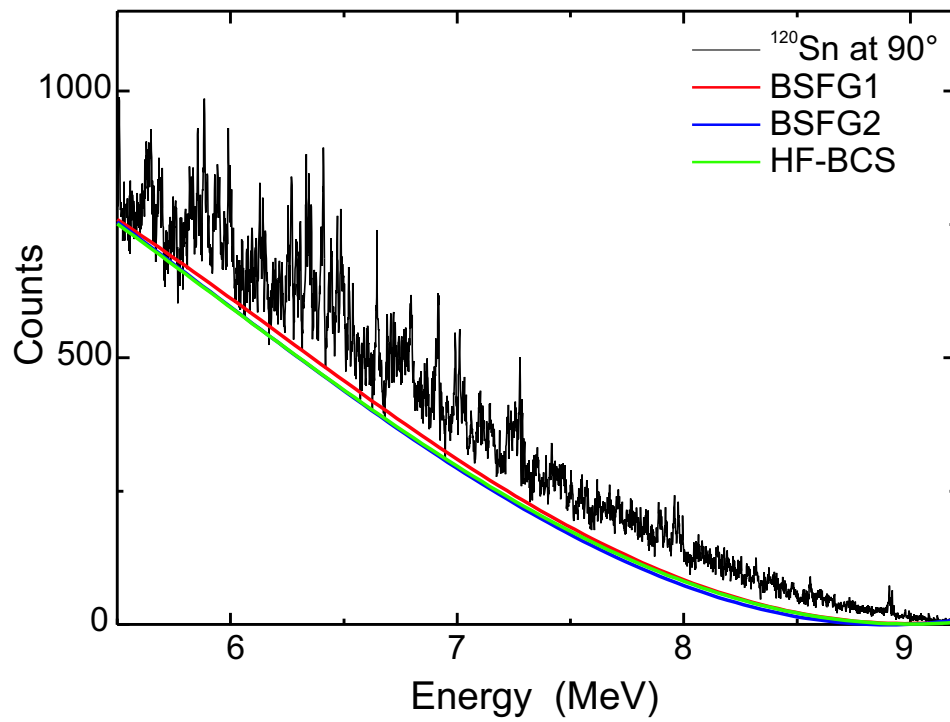
Figure 4.17 ^{120}Sn spectrum at 90° and calculated backgrounds according to the BSFG1, BSFG2 and HF-BCS level density models
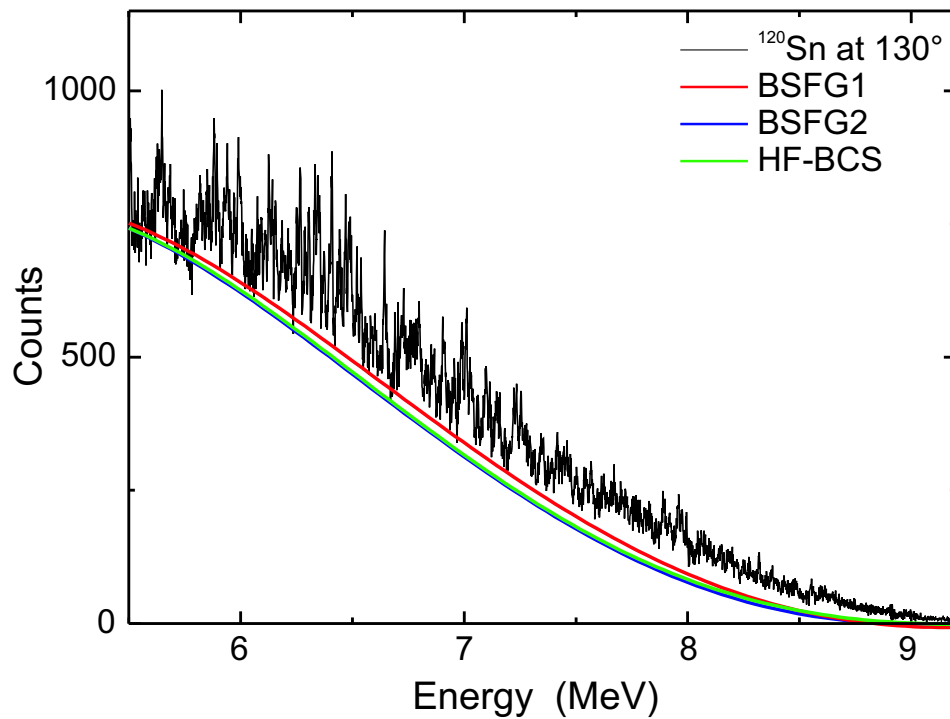

Figure 4.18 ^{120}Sn spectrum at 130° and calculated backgrounds according to the BSFG1, BSFG2 and HF-BCS level density models
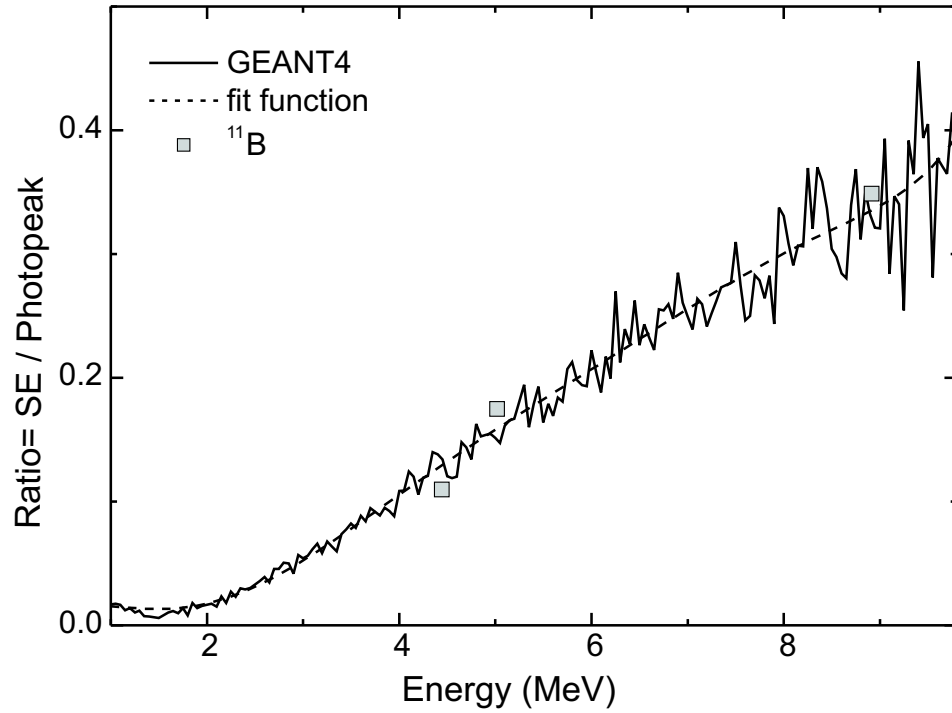
Figure 4.19   GEANT4 simulation of the ratio of SE to photopeak as a function of the gamma energy, a fit function (dashed line) and a comparison to experimentally measured ratios in ^{11}B (grey squares).

Table 4.5   Results of the fluctuation analysis and the NRF analysis

	total (e^2fm^2)	unresolved (e^2fm^2)	resolved (e^2fm^2)
$\sum$B(E1) for ^{112}Sn	0.255(16)	0.113(16)	0.142(18)
$\sum$B(E1) for ^{120}Sn	0.253(33)	0.120(33)	0.133(25)

comparison with experimentally determined ratios for ^{11}B transitions. The fit function is used for an energy-dependent correction of the integrated cross sections per energy interval. The calculated total strengths, the sum of unresolved strengths from fluctuation analysis and the sum of resolved strengths from the first analysis (explained in Chapter 3) are listed in Table 4.5. Errors of unresolved and total strengths are determined by the differences between the results from the three NLD models. In the energy region E_x= 5.5-7.8 MeV, the unresolved strengths amount to 44 % and 47 % of the total strength are observed in the NRF spectra of ^{112}Sn and ^{120}Sn, respectively. The amount of unresolved

strengths are very similar because, as seen from Fig. 4.13 and Fig. 4.14 the level spacings of ^{112}Sn and ^{120}Sn show similar value with energy.

5. DISCUSSION and CONCLUSION

5.1   Comparison with Theoretical Models

5.1.1   Quasiparticle Phonon Model (QPM)

The measured B(E1) transition strengths below the neutron threshold in stable tin iso-topes are compared with theoretical models in this section. In particular, the QPM and R QRPA are used for the comparison. The tin isotopic chain has been studied systematically in both approaches.

The present QPM model approach is described in (Tsoneva et al., 2004a; 2004b; 2007). The model Hamiltonian is written as

$$H = H_{MF} + H_M^{ph} + H_{SM}^{ph} + H_M^{pp} \tag{5.1}$$

Here, $H_{MF}=H_{sp}+H_{pair}$ is the mean field part consisting of a single-particle (H_{sp}) and a pairing (H_{pair}) part which has to be identified with the Hartree-Fock Bogoliubov (HFB) Hamiltonian. The calculation uses single-particle energies, wave functions obtained self-consistently and a reparameterization of the HFB mean field in terms of a Woods-Saxon potential as described in (Tsoneva at al., 2004b).

The QPM calculations in $^{110-132}$Sn contain a sequence of low-lying one-phonon 1-states at excitation energies E_x = 6 - 7.5 MeV which shows almost pure neutron structure with proton contributions of less than 1%. The main part of the PDR comes from one-, two- and three quasiparticle states in this type of nonrelativistic calculations. The predicted excitation energies of these states also define the energy region of the PDR. The results for ^{120}Sn are displayed in Fig 5.1. The quantity R is an amplitude which is entering in the definition of the multi-phonon wave function. The square of it is a probability to have a certain one-phonon contribution to the structure of an excited state. As seen from the figure the PDR is concentrated in the energy region 6.5 - 7.5 MeV for this isotope. Calculations for other even tin isotopes show almost the same energy region for the PDR (Tsoneva, et al., private com.).

The results of a calculation with 240 one-, two- and three phonon configurations
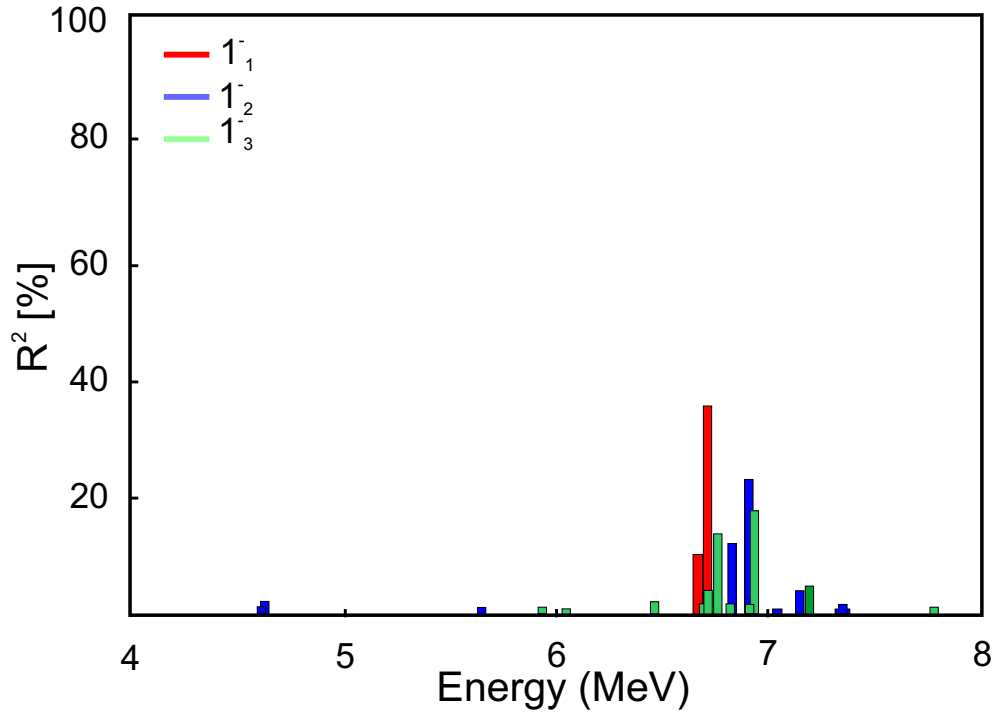
Figure 5.1   Distriution of the strength of pure neutron one-phonon transitions in QPM calcula-
tions with up to 3 phonon confi gurations for ^{120}Sn

Table 5.1   Results of QPM calculations up to 3 phonon confi gurations for the summed B(E1)
strength and the centroid energy of the PDR

Isotope	$\sum$B(E1)(e^2fm^2)	E_C (MeV)
^{112}Sn	0.145	7.90
^{114}Sn	0.165	7.70
^{116}Sn	0.209	7.20
^{118}Sn	0.229	7.10
^{120}Sn	0.259	6.88
^{122}Sn	0.270	6.70
^{124}Sn	0.310	6.68

(Tsoneva, et al., 2007) are given in Table 5.1 for the stable tin isotopes.

Another QPM calculation has been performed (Ponomarev, private com.) allowing for
a very large model space. It slightly differs in the treatment of the mean field, since the
single-particle states are determined in a Woods-Saxon potential obtained from a global
fit to spherical nuclei over a wide mass range (Ponomarev et al., 1979). This calculation

Figure 5.2   Upper part: E1 strength distribution measured in the ^{112}Sn (γ,γ') reaction. Lower part: QPM calculation using a large multiphonon configuration space. The solid line is the sensitivity limit of experiment.

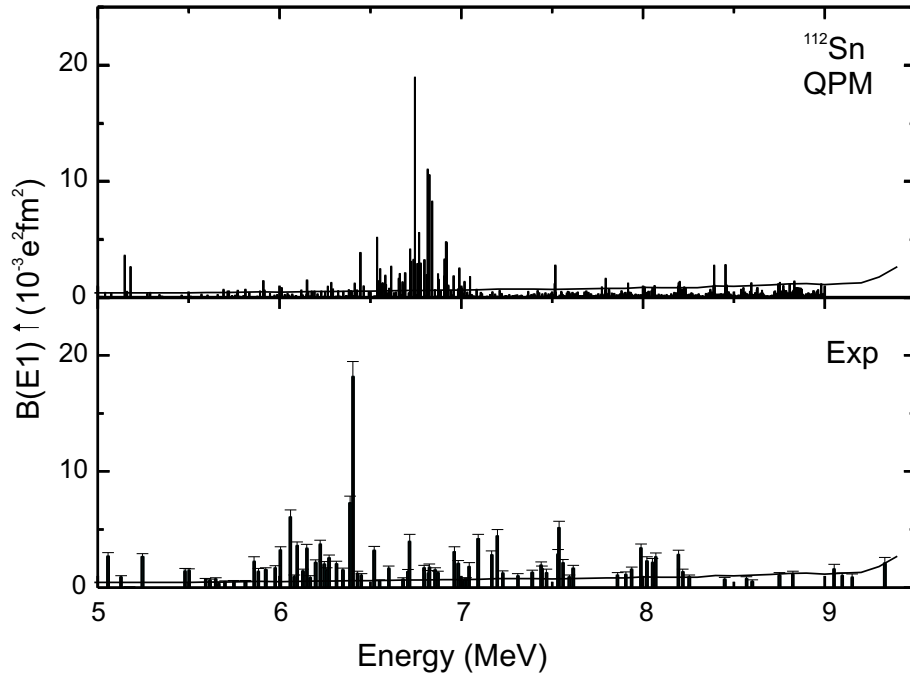Figure 5.3   Upper part: E1 strength distribution measured in the ^{120}Sn (γ,γ') reaction. Lower part: QPM calculation using a large multiphonon configuration space. The solid line is the sensitivity limit of experiment.
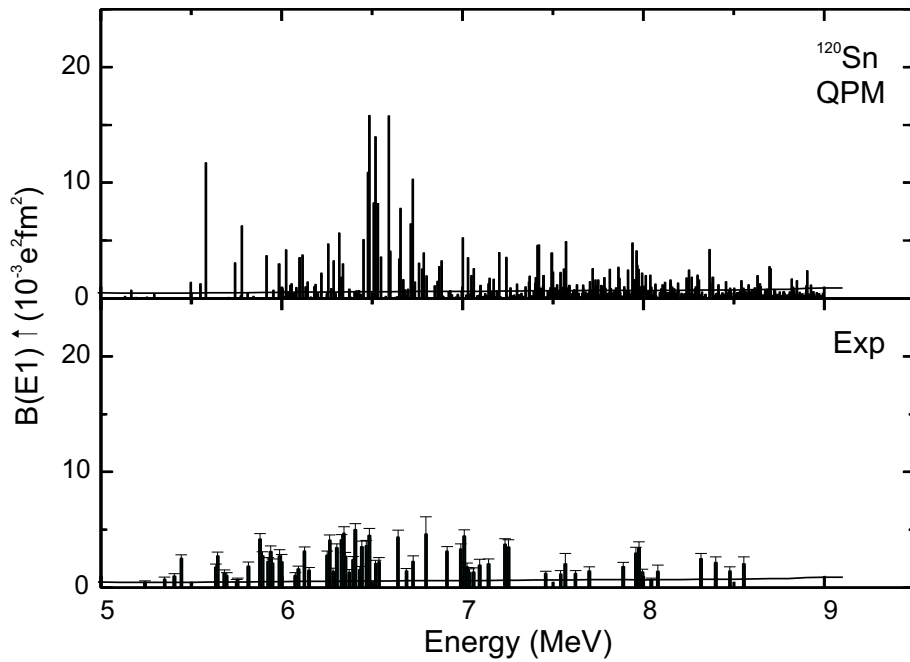
includes all possible transitions up to three phonons. This allows to test the experimentally observed strong fragmentation. The measured and predicted transitions are displayed for ^{112}Sn in Fig. 5.2 and for ^{120}Sn in Fig. 5.3. As seen in Fig. 5.2, the QPM calculation shows good agreement with the experimental results of ^{112}Sn(γ,γ') except a small shift of the centroid. The solid line in the figures show the experimental sensitivity limit. The QPM calculation predicts a lot of transitions smaller than this limit which correspond to approximately 15 % of total predicted strength in both isotopes. The rest of predicted strengths are still more than observed experimentally. The stronger experimental fragmentation is especially visible in the comparison for ^{120}Sn shown in Fig. 5.3.

5.1.2 Relativistic Quasiparticle Random Phase Approximation (R QRPA)

The R QRPA calculation is based on the single-particle basis obtained in a self-consistent relativistic Hartree-Bogoliubov (RHB) approach and uses an interaction with density-dependent meson-nucleon couplings, called DD-ME2 (Paar et al., 2005). The RHB model provides a unified describtion of parcticle-hole (ph) and particle-particle (pp) correlations. The results of the R QRPA calculation for the summed B(E1) strengths and the centroid energies of the PDR in stable tin isotopes are listed in Table 5.2.

Table 5.2   Results of R QRPA calculations for stable even tin isotopes

Isotope	$\sum$B(E1)(e^{2}fm^2)	E_C (MeV)
^{112}Sn	0.285	9.33
^{114}Sn	0.548	9.22
^{116}Sn	0.917	9.11
^{118}Sn	1.483	9.07
^{120}Sn	1.822	8.92
^{122}Sn	2.085	8.79
^{124}Sn	2.393	8.75

5.1.3   Discussion

The experimental summed B(E1) strengths and centroid energies for ^{112,116,120,124}Sn are compared to the theoretical QPM and R QRPA calculations (Tsoneva et al., 2007; Paar et al., 2005) summed over an energy region E_x= 5.5-7.8 MeV in Fig 5.4. In this figure the open triangles are R QRPA calculations, the upturned triangles are QPM calculations, the full circles are the experimental results for ^{112,120}Sn from the analysis of discrete transitions, the full squares are total strengths of ^{112,120}Sn which consists of measured B(E1) strength and unresolved strength from the fluctuation analysis and the stars are the sum of measured B(E1) strengths of ^{116,124}Sn (Govaert, et al., 1997).

The upper part of the Fig. 5.4 shows the comparison of centroid energies as a function of mass number. The results of the R QRPA calculation are much higher than the experimental results and the QPM values. Both models predict that the centroid energies decreases with the number of neutrons. Although the experimental results are closer to the QPM calculation, they do not exhibit such a smooth dependence on the neutron number. On the contrary, the experimental results show almost constant values in every isotope. Including the unresolved strength has little effect on the centroid energies.

The lower part of Fig. 5.4 displays the sum of B(E1) transition strengths as a function of mass number in two different scales because R QRPA predicts much higher strengths compared to the results of experiments and QPM calculations. The R QRPA calculations do not show agreement with experimental results except the corrected total strength of ^{112}Sn. There is another R QRPA calculation is not shown in Fig. 5.4, but predicts almost the same amount of E1 strength in tin isotopes (Piekarewicz, 2006) with that from Paar (Paar et al., 2005). The much larger strength and higher centroid energy in these calculations indicate that the effective mass used in this model, which scale the single-particle spectrum, are not correct.

Both theoretical calculations (QPM and R QRPA) predict that the sum of B(E1) strengths should increase with the number of neutrons. The QPM calculations are relatively close the experimental results. Without unresolved strength correction the ^{112,116,124}Sn isotopes show good agreement with QPM predictions but ^{120}Sn would be too small. After the correction, the sum of strengths of ^{112}Sn and ^{120}Sn are increasing by almost 50 %. Now, ^{120}Sn is in good agreement but ^{112}Sn would be underpredicted by the

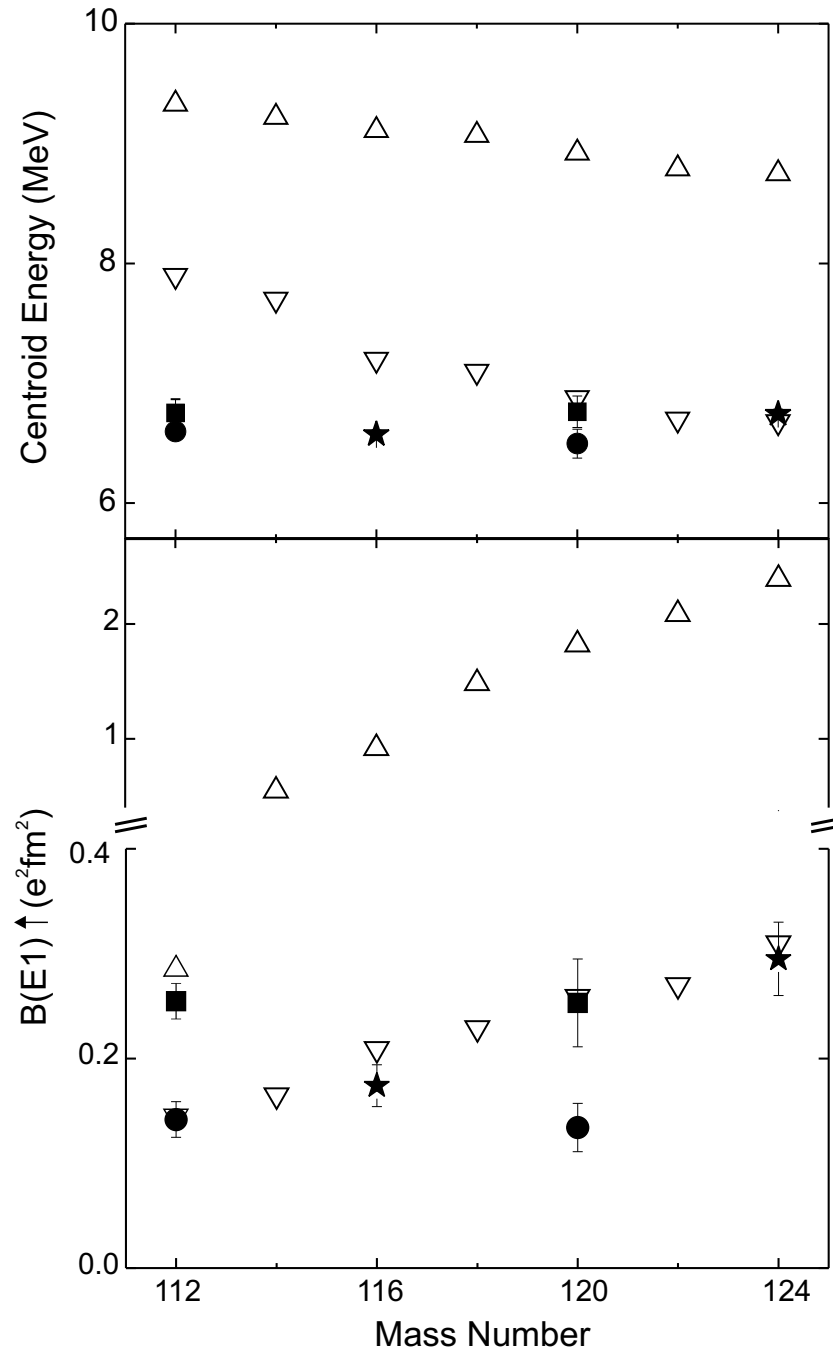Figure 5.4   Comparison of R QRPA (triangles) and QPM (upturned triangles) calculations of the PDR centroid energies (upper part) and summed B(E1) strength (lower part) to the experimental results in ^{112,116,120,124}Sn. Circles: Resolved transitions in ^{112,120}Sn from present work. Stars: Resolved transitions in ^{116,124}Sn (Govaert et al., 1997). Squares: Total strength including unrsolved transitions from present work.

QPM. For a realistic comparison one should also know the unresolved strength of ^{116,124}Sn isotopes. As mentioned before in the fluctuation analysis method the selection of background in (γ, γ') spectrum depends on the mean level spacing of nucleus under consideration. In this case the amount of unresolved strengths of ^{116,124}Sn isotopes can be expected to be similar to that of ^{112,120}Sn. In such a case, the total strength of ^{120}Sn would still be lower than other experimental corrected values. Thus, the present work indicates that the PDR does not depend directly on the neutron excess.

However, there is an experimental problem since the present measurements are not sensitive over the full energy region where the PDR is predicted, and omitted inelastic branchings might become important at higher energies. On the other hand the QPM results support that the PDR is confirmed to the energy region, where strength is observed in the (γ, γ') For a final conclusion one needs a consistent set of data of the E1 response from low to high energies as a real test of the models.

5.2 Conclusion and Outlook

In summary, the thesis presents high-resolution nuclear resonance fluorescence experiments on ^{112}Sn and ^{120}Sn stable isotopes to investigate the E1 response below the neutron threshold. The strongest transitions have been observed around the energy region of 6-7 MeV and the distributions of extracted B(E1) transitions have a resonance-like structure, but in the case of ^{120}Sn the dipole strengths are more fragmented. The sum of B(E1) strengths are 187 (24) e^{2}fm^2 and 164 (29) e^{2}fm^2 with centroid energies 6.7 MeV and 6.6 MeV for ^{112}Sn and ^{120}Sn, respectively.

A fluctuation analysis was applied to the (γ, γ') spectra to estimate the unresolved strength which might be hidden in the background due to the finite energy resolution. This analysis have been performed with the help of an autocorrelation function which provides the information about the mean level spacing in the defined energy intervals. These can be compared to model prediction of the NLD, which allows to adjust the background. Three different theoretical models explained in Chapter 4 have been used: BSFG1, BSFG2 and HF-BSC (Egidy et al., 2005; Rauscher, et al., 1997; Demetriou et al., 2001). The backgrounds determined from these models produce a very similar amount of unresolved strength in the spectra and the differences between the models have been used to deter-

mine the uncertainties of this procedure. The fluctuation analysis shows that the amount of unresolved strength on (γ,γ′) spectra is obviously not negligible and should be applied to other data which are taken with the NRF method, i.e. the spectra of ^{116}Sn and ^{124}Sn. Together with the so determined unresolved part, the measured B(E1) strength distributions below the neutron threshold in ^{112}Sn and ^{120}Sn was compared to microscopic model to understand their nature. QPM calculations with a very large multiphonon configuration (Ponamarev, private com.) reasonably reproduce the fragmentation of the transition strengths for ^{112}Sn and ^{120}Sn. The QPM and the R QRPA calculations predict a smooth increase of the summed B(E1) strength and a decrease of the centroid energy with neutron number in stable tin isotopes. However, the experimental results do not show a simple dependence on neutron excess. This indicates that the low-energy E1 strength retains much of its single-particle character rather than developing into a true collective mode. This is in agreement with the picture deduced from the QPM results but contradicts the R QRPA results.

For an improved understanding measurements of the complete E1 response below and above the neutron threshold would be important. This is possible with high resolution (p,p′) experiment at 0° at RCNP Osaka university (Tamii et al., 2007) and also in near future in photon scattering experiments with new NEPTUN tagger facility at the S-DALINAC (Lindenberg, 2007).

REFERENCES

AAB V. et al., Proc. 3rd Workshop on Rf Supercond., Ed. K.W.Shepard, ANL-Phy-88-1 (1988) 127.

ADAMS, J. P. et al., Phys. Rev. C 53 (1996) 1016

ADRICH, P. et al., Phys. Rev. Lett. 95 (2005) 1325

——————————, Dissertation, Jagiellonian University, 2005

AUDI, G., WAPSTRA, A. H.and THIBAULT, C., Nucl. Phys. A 729, 337 (2003)

AUERHAMMER, J. et al., Nucl. Phys. A553 (1993) 841c

AUERHAMMER, J. et al., Proc. 5thWorkshop on Rf Supercond., Ed. D.Proch, DESY M-92-01 (1992) 110

AUMANN, T., Eur. Phys. J. A 26 (2005) 441

BALBUTSEV, E. B. et al., Europhys. Lett. 26 (1994) 499

BALDWIN, G. C., KLEIBER, G. S., Phys. Rev. 71 (1947) 3

BARTHOLOMEV, G. A. et al., Adv. Nucl. Phys. 7 (1972) 229.

BASTRUKOV, S. I. et al., Nucl. Phys. A562 (1993) 191

BAUWENS, F. et al., Phys. Rev. C 62 (2000) 024302

BEAUSANG, C. W. and SIMPSON J., J. Phys. G: Nucl. Part. Phys. 22 (1996) 527

BERG U. E. P. et al., Phys. Lett. B 103 (1981) 301

BERMAN, B. L., FULTZ, S. C., Rev. Mod. Phys. 47 (1975) 713

BETHE, H. A. and PLACZEC, G., Phys. Rev 51 (1937) 450

BOHR, A. and MOTTELSON, B.R. Nuclear Structure, Vol.2, Nuclear Deformations, W.A.Benjamin, Advanced Book Program, Massachusetts, (1975)

BOTHE, W., GENTNER, W., Z. Phys. 71 (1937) 236

BROWN, G.E. and BOLSTERLI, M., Phys. Rev. Lett. 3 (1959) 472

BRYSSINCK, J. et al., Phys. Rev. C 59 (1999) 1930

CHAMBERS, J. et al., Phys. Rev. C 50 (1994) R2671

CHAPURAN, T. , VODHANEL, R., BRUSSEL, M. K., Phys. Rev. C 22 (1980) 1420

COLÒ, G. et al., Phys. Lett. B 485 (2000) 362

DEMETRIOU, P. and GORIELY, S., Nucl. Phys. A 695 (2001) 95

DIETRICH, S. S., BERMAN., B. L., At. Data Nucl. Data Tables 38 (1988) 199

ENDERS, J. et al., Nucl. Phys. A 636 (1998) 139

——————————, Nucl. Phys. A 724 (2003) 243

——————————, Phys. Lett. B 486 (2000) 279

——————————, Phys. Rev. C 57 (1998) 996

——————————, Phys. Rev, Lett. 79 (1997) 2010

ERICSON, T., Adv. Phys. 9 (1960) 425

FUKUNISHI, N. , OTSUKA, T. , TANIHATA, I., Phys. Rev. C 48 (1993) 1648

GEIGER, W. et. al., Nucl. Phys. A 580 (1994) 263

GILBERT, A. and CAMERON, A. G., Can. J. Phys. 43 (1965) 1446

GOLDHABER, M., TELLER, E., Phys. Rev. 74 (1948) 1046

GORIELY, S., TONDEUR, F. and AERSON, J.M., At. Data Nucl. Data Tables 77 (2001) 311

GOVAERT, K. et al., Phys. Rev. C 57 (1997) 2229

GRINBERG, M. and STOYANOV, C., Nuclear Phys. A 573 (1994) 231

GUHR, T., MUELLER-GROELING and A., WEIDENMUELLER, H.A., Phys. Rep. 299 (1998)189

HANSEN, P. G., Annu. Rev. Nucl. Part. Sci. 29, 69 (1979)

HARAKEH, M. N. and van der WOUDE, A., Giant Resonances, Oxford Studies in Nuclear Physics, Vol. 24 (Oxford University Press, 2001)

HARTMANN, T. et al., Phys. Rev. Lett. 85 (2000) 274

HASPER, J., private communication (2007)

HERZBERG, R. D. et al., Phys. Rev. C 60 (1999) 051307(R)

HUXEL, N., et al., Nucl. Phys. A 645 (1999) 239

——————————, dissertation TH Darmstadt (1997)

IACHELLO, F., Phys. Lett. 160B (1985) 1

IGNATYUK, A.V., ISREKOV, K. K. and SMIRKENKIN, Sov. J. Nucl. Phys. 29 (1979) 450

IGNATYUK, A.V., SMIRKENKIN, G.N. and TISHIN, A. S., Sov. J. Nucl. Phys. 21 (1975) 255

ILJINIV, A. S. et al., Nucl. Phys. A543 (1979) 450

HASPER, J., private communication

JONSON, B. et al., Proceedings of the 3rd International Conference on Nuclei far from Stability, Cargese, 1976, CERN Report No. 76-13 (1976) p. 277.

KÜBLER, L. et al., Phys. Rev. C 70 (2004) 064307

KALMYKOV, Y. et al., Phys. Rev. Lett. 96 (2006) 012502

——————————, Phys. Rev. Lett. 99 (2007) 202502

KILGUS, G. et al., Z. Phys. A 326 (1987) 41

KLIMKIEWICZ, A. et al., Phys. Rev. C 76 (2007) 051603(R)

KNEISSL, U., PITZ, H. H. and ZILGES, A., Prog. Part. Nucl. Phys. 37 (1996) 349

KNEISSL, U., PIETRALLA, N. and ZILGES, A., J. Phys. G: Nucl. Part. Phys. 32 (2006) R217

KRASZNAHORKOY, A. et al., Phys. Rev. Lett. 66 (1991) 1287

LINDENBERG, K., Dissertation, TU Darmstadt (2007)

LIPAS, P. O., Nucl. Phys. 82 (1966) 91

LONGORIA, L. C. et al., Nucl. Inst. Meth. Phys. Res. A 229 (1990) 308

METZGER, F. R., FRISCH, O. R., Progress in Nuclear Physics, London, Vol. 7, (1959)

MIGDAL, A., J. Phys. (USSR) 8 (1944) 331

MISIÇU, S. and S. I. BASTRUKOV, Eur. Phys. J. A 13 (2002) 399

MOHAN, R. et al., Phys. Rev. C 3 (1971) 1740

MOHR, P. et al., Nucl. Inst. Meth. Phys. Res. A 423 (1999) 480

MÖLLER, P. et al., At. Data Nucl. Data Tables 59 (1995) 185

MÜLLER, S. et al., Phys. Lett. 113B (1982) 362

MYERS, W. D., SWIATECKI, W. J. and Wang, C. S., Nucl. Phys. A436 (1985) 185

NNDC, http://www.nndc.bnl.gov/ (2007)

OROS, A. M. et al., Phys. Rev. C 57 (1998) 990

PAAR, N. et al., Phys. Lett. B 606 (2005) 288

——————————, Phys. Rev. C 67 (2003) 034312

PIEKAREWICZ, J., Phys. Rev. C 73 (2006) 044325

PIETRALLA, N. et al., Phys. Rev. Lett. 88 (2002) 012502

PONOMAREV, V.Yu. et al., Nucl. Phys. A 323 (1979) 446

——————————————, private communication

PORTER, C. E. and THOMAS, R. G., Phys. Rev. 104 (1956) 483

PYSMENETSKA, I. et al., Phys. Rev. C 73 (2006) 17302

RAUSCHER, T., THIELEMANN, F.-K. and KRATZ, K.,-L., Phys. Rav. C 56 (1997) 1613

RICHTER, A., Proceeding of the Fifth European Particle Accelerator Conference, ed. S. Meyers et al., (IOP Publishing, Bristol, 1996) 110.

——————————, Nucl. Phys. A 522 (1991) 139c.

RYEZAYEVA, N. et al., Phys. Rev. Lett. 89 (2002) 272502

STEINWEDEL, H. and JENSEN J. H. D., Phys. Rev. 74 (1950) 1019

SUZUKI, Y. et al., Prog. Theor. Phys. 83 (1990) 180

SCHWENGNER, R. et al., Phys. Rev. C 76 (2007) 034321

——————————————, Nucl. Phys. A 788 (2007) 331c

TAMII, A. et al., Nucl.Phys. A 788, 53 (2007)

TERASAKI, J. et al., Phys. Rev. C 71 (2005) 034310

TONDEUR, F. et al., Phys. Rev. C 62 (2000) 024308

TSONEVA, N., LENSKE, H., STOYANOV, Ch., Nucl. Phys. A 731 (2004)a 273

————————, Nucl. Phys. A 586 (2004)b 213

TSONEVA, N. and LENSKE, H., arXiv:0706.4204v1 [nucl-th] 28 Jun 2007

Van ISACKER, P. et al., Phys. Rev. C 45 (1992) R13

VOGEL, P. and KOCHBACH, L., Nucl. Phys. A 176 (1971) 33

VOLZ, S. et al., Nucl. Phys. A 779 (2006) 1

————————, private communication

von EGIDY, T. and BUCURESCU, D., Phys. Rev. C 72, 044311(2005)

VRETENAR, D. et al., Phys. Rev. Lett. 91 (2003) 262502

——————————————, Phys. Rev. C 65 (2002) 021301

——————————————, Phys. Lett. B 487 (2000) 334

WIGNER, E. P., in: C. E. Porter (Ed.), Statistical Theories of Spectra: Fluctuations (Academic Press, New York, 1965) 200.

WONG, S. S. M., Introductory Nuclear Physics (Prentice-Hall International, Inc. 1990)

ZHONGFU, H. et al., Chin. J. Nucl. Phys. 13 (1941) 147

ZILGES, A. et al., Phys. Lett. B 542 (2002) 43

CURRICULUM VITAE

Name   : Banu Özel

Date of Birth   : 25.08.1976

Nationality   : Turkish

EDUCATIONAL BACKGROUND

1994-1998   : B.Sc Ankara University

2000-2003   : M.Sc Çukurova University

2003-2008   : Ph.D Çukurova University

PROFFESSIONAL BACKGROUND

Mar. 1999 - Nov. 2000   : research assistant at Nigde University

Nov. 2000 - now   : research assistant at Çukurova University

Oct.2004 - July 2005   : guest student in Institut für Kernphysik

                                               TU-Darmstadt, Germany with Erasmus Program

Aug. 2005 - Oct. 2007   : guest student in Institut für Kernphysik

                                               TU-Darmstadt, Germany with DAAD Scholarship